

Improved sensitivity and quantification for ^{29}Si NMR experiments on solids using UDEFT (Uniform Driven Equilibrium Fourier Transform)

Nghia Tuan Duong,^{1,#} Julien Trébosc,^{1,2*} Olivier Lafon,^{1,3} Jean-Paul Amoureux^{1,4*}

¹ Univ. Lille, Centrale Lille, ENSCL, Univ. Artois, CNRS-8181, UCCS – Unit of Catalysis and Chemistry of Solids, F-59000 Lille, France.

² Univ. Lille, CNRS-FR2638, Fédération Chevreul, F-59000 Lille, France.

³ Institut Universitaire de France, 1 rue Descartes, F-75231 Paris, France.

⁴ Bruker Biospin, 34 rue de l'industrie, F-67166 Wissembourg, France.

Present address: RIKEN-JEOL Collaboration Center, Yokohama, Kanagawa 230-0045, Japan.

Email addresses: julien.trebosc@univ-lille.fr jean-paul.amoureux@univ-lille.fr

Abstract. We demonstrate the possibility to use UDEFT (Uniform Driven Equilibrium Fourier Transform) technique in order to improve the sensitivity and the quantification of one-dimensional ^{29}Si NMR experiments under Magic-Angle Spinning (MAS). We derive an analytical expression of the signal-to-noise ratios of UDEFT and single-pulse (SP) experiments subsuming the contributions of transient and steady-state regimes. Using numerical spin dynamics simulations and experiments on ^{29}Si -enriched amorphous silica and borosilicate glass, we show that $59_{180}298_059_{180}$ refocusing composite π -pulse and the adiabatic inversion using tanh/tan modulation improve the robustness of UDEFT technique to rf-inhomogeneity, offset, and chemical shift anisotropy. These pulses combined with a two-step phase cycling limit the pulse imperfections and the artifacts produced by stimulated echoes. The sensitivity of SP, UDEFT and CPMG (Carr-Purcell Meiboom-Gill) techniques are compared experimentally on functionalized and non-functionalized mesoporous silica. Furthermore, experiments on a flame retardant material prove that UDEFT technique provides a better quantification of ^{29}Si sites with higher sensitivity than SP method.

Keywords. Quantitative NMR, DEFT, UDEFT, CPMG, ^{29}Si , long T_1 .

I Introduction

^{29}Si NMR spectroscopy has been used for the characterization of a wide range of solids, including silicon alloys [1–4], silicon-containing organic compounds [5,6] and polymers [7], silicon nitride and carbide ceramics [8,9], crystalline and amorphous silicates, including minerals [10–12], zeolites [13,14], cements [15,16], silica-supported catalysts [17–19], acid heterogeneous catalysts made of amorphous aluminosilicates [20] and glasses [21–23]. ^{29}Si is a spin-1/2 isotope, but its NMR sensitivity is small due to its low natural abundance (4.7 %), its moderate gyromagnetic ratio ($\gamma_{^{29}\text{Si}} \approx 0.2\gamma_{^1\text{H}}$) and its very long longitudinal relaxation times, T_1 , which can reach tens of hours [24,25].

Various approaches have been proposed to enhance the NMR sensitivity of ^{29}Si nuclei. The CPMG (Carr-Purcell Meiboom-Gill) sequence [26], which consists of an excitation pulse followed by a train of spin-echoes (Fig. 1d), allows the acquisition of multiple echoes in every scans [27,28]. These echoes result from the refocusing of the inhomogeneous broadening of ^{29}Si signal, produced especially by the distribution of isotropic chemical shifts in disordered solids. However, when the flip-angle of the refocusing pulses is distinct from π , they can convert the transverse magnetization into longitudinal one and create stimulated echoes that may pollute the CPMG signal [29,30]. A variant of CPMG, named PIETA (Phase-Incremented Echo-Train Acquisition), has been introduced to suppress the contribution of the stimulated echoes and has been applied to separate isotropic and anisotropic chemical shifts or to measure the $J_{^{29}\text{Si}-^{29}\text{Si}}$ couplings [30–32].

In the case of sites exhibiting different decay times, CPMG spectra are not directly quantitative. However, quantitative information can then be retrieved by measuring these decay times for the different sites [33]. Nevertheless, this approach is only applicable in the case of high signal-to-noise (S/N) ratio.

For protonated solids, another strategy to enhance the ^{29}Si sensitivity is to transfer the polarization of protons to ^{29}Si nuclei using CPMAS (Cross-Polarization under Magic-Angle Spinning) sequence [34,35]. The sensitivity gains of this experiment stem from the larger polarization and faster longitudinal relaxation of protons with respect to ^{29}Si nuclei. Furthermore, the sensitivity of $^1\text{H} \rightarrow ^{29}\text{Si}$ CPMAS has been further enhanced by using CPMG detection [36]. Recently $^1\text{H} \rightarrow ^{29}\text{Si}$ multiple-contact CPMAS scheme has also been applied to record quantitative ^{29}Si NMR spectra [37].

Correspondingly, the sensitivity of ^{29}Si NMR can also be enhanced by DNP (Dynamic Nuclear Polarization) under MAS, i.e. the microwave-driven transfer of polarization from unpaired electrons to ^{29}Si nuclei. This approach has been demonstrated first at low static magnetic field $B_0 = 1.4$ T [38], and more recently at $B_0 \geq 9.4$ T [39–41]. DNP can be combined with either $^1\text{H} \rightarrow ^{29}\text{Si}$ CPMAS [39], its multiple contact version [41], or CPMG [42].

Here, we propose the use of UDEFT (Uniform Driven Equilibrium Fourier Transform) technique (Fig. 1b) to enhance the NMR sensitivity of ^{29}Si on solids, without resorting to polarization transfer. Like CPMG, UDEFT can be applied for non-protonated samples and does not require the additional presence of polarizing agents into the sample. The UDEFT scheme derives from the DEFT (Driven Equilibrium Fourier Transform) sequence (Fig. 1a) [43]. The DEFT sequence consists of a spin-echo followed by a flip-back pulse, which returns the transverse magnetization to the z -axis after the acquisition. This sequence has been applied for the NMR acquisition of slowly relaxing nuclei, such as ^{13}C or ^{29}Si , in solutions [44,45]. It has also been used to suppress the signal of water in NMR spectroscopy [46] or to accelerate the acquisition of images in magnetic resonance microscopy and imaging by driving back the magnetization of water toward the z -axis [47,48]. However, DEFT is sensitive to radio-frequency (rf) field inhomogeneities and resonance offsets [49–52]. It has been shown that the UDEFT variant using adiabatic π -pulses circumvents this issue and is widely used for the direct excitation of ^{13}C spectra [53]. Nevertheless, to the best of our knowledge, neither DEFT nor UDEFT techniques have been used so far to acquire NMR spectra of solids.

We demonstrate here that UDEFT enhances the sensitivity for the NMR detection of ^{29}Si nuclei in solids and improve the quantification of ^{29}Si sites. We derive the analytical expression of the S/N ratio of UDEFT by taking into account the contributions of transient and steady-state signals. We also determine the minimum recycle delay for the acquisition of quantitative UDEFT spectra and their S/N ratios. Using numerical simulations and experiments on ^{29}Si labeled amorphous silica and borosilicate glass, we analyze the robustness to the synchronization with the sample rotation, rf-inhomogeneity, offset and CSA (Chemical Shift Anisotropy). This analysis allows selecting the optimal phases for the pulses and the most robust composite or adiabatic π -pulses to refocus or invert the ^{29}Si magnetization in the UDEFT sequence. ^{29}Si experiments on unlabeled mesoporous silica samples are used to compare the sensitivity of UDEFT, single-pulse (SP) and CPMG techniques. SP and UDEFT experiments are also compared to quantify the relative amount of di- (D: SiO_2C_2) and tri-functional (T: SiO_3C) sites in silicon resin with flame retardant properties.

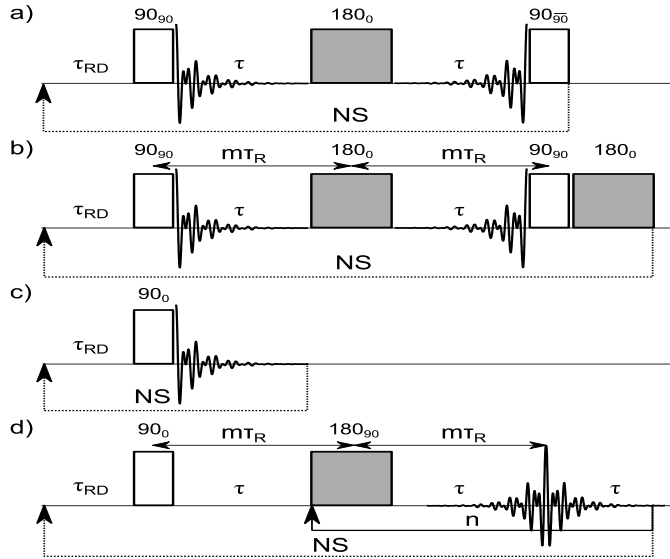


Fig.1. Pulse sequences of (a) DEFT, (b) UDEFT, (c) SP, and (d) spin-echo/CPMG experiments. The white and dark rectangles represent the $\pi/2$ - and π -pulses, respectively. T_R denotes the rotor period, τ_{RD} the recycle delay, τ the echo delay, which is rotor synchronized with respect to the middle to the surrounding pulses. NS is the number of scans, and n the number of acquired echoes in CPMG. For UDEFT experiments, a two-step phase cycle is employed: the phases of the refocusing and inversion pulses are incremented by 180° , whereas that of the receiver remains constant. The length of each rf element is called τ_p in the following.

II UDEFT sequence

The original DEFT sequence, shown in Fig.1a, can be written as: $90_{90} - \tau$ (sampling) $- 180_0 - \tau - 90_{-90}$ [43], where τ is the echo delay and θ_ϕ denotes a rectangular, resonant pulse with flip-angle θ and phase ϕ , both values given in degrees. The first $\pi/2$ -pulse flips the magnetization from the z - to the x -axis. The NMR signal is detected during the first τ delay. The central π -pulse refocuses the evolution under the isotropic chemical shifts and the transverse magnetization points toward the x -axis at the end of the second τ delay. Then, the second $\pi/2$ -pulse returns the magnetization back to the initial z -axis. In the case of ideal pulses and without relaxation, the longitudinal magnetization after the second $\pi/2$ -pulse is equal to the magnetization at thermal equilibrium and the DEFT scheme can be repeated indefinitely without signal decay. However, experimental pulse imperfections and relaxation lead to magnetization losses and the signal detected during each scan decreases for an increasing number of scans.

The UDEFT sequence shown in Fig.1b can be written as $[90_{90} - \tau$ (sampling) $- 180_0 - \tau - 90_{90}] 180_0$ [53]. In UDEFT, both $\pi/2$ -pulses have identical phases. Such modification improves the robustness to rf-inhomogeneity since for resonant irradiation, the UDEFT sequence mimics the behavior of the $90_{90}180_090_{90}$ composite pulse [54,55] to invert the magnetization. It must be emphasized here that even if the first three pulses of the sequence are those of this $90_{90}180_090_{90}$ composite pulse, the UDEFT sequence by itself does not behave as a composite pulse; it is only inspired by it. However, as will be seen in the following the UDEFT sequence is much more robust than the DEFT one. After the second $\pi/2$ -pulse, the magnetization points toward the $-z$ direction and a second π -pulse is employed to return the magnetization back to the initial z -axis.

For solution-state experiments, the refocusing element of UDEFT was a composite adiabatic π -pulse made of three smoothed Chirp pulses with relative lengths of $\tau_p/4$, $\tau_p/2$ and $\tau_p/4$ [56], whereas the inversion pulse was a single smoothed Chirp adiabatic pulse [57]. In the case of rotating solids, the CSA produces an additional modulation of the resonance frequency, which can interfere with the sweep of the frequency offset during adiabatic pulses. Consequently, these pulses in solids are only efficient for moderate CSA and MAS frequencies or when they are short with high rf-power [58–60]. Therefore, alternatives to smoothed Chirp adiabatic pulses were tested with refocusing and inversion

composite π -pulses and these are listed in Tables S1 and S2, respectively. As refocusing element, we also tested several composite tanh/tan adiabatic pulses, including the BIR-4 (B_1 -Insensitive Rotation) one [61,62] and three successive such pulses with relative lengths of $\tau_p/4$, $\tau_p/2$ and $\tau_p/4$ [56]. For the inversion element, we also employed the tanh/tan adiabatic pulse, which has been developed to achieve fast broadband inversion and has been applied to solid-state experiments [63,64].

During a tanh/tan pulse with a length τ_p , the instantaneous rf-amplitude is equal to

$$v_1(t) = \begin{cases} v_{1\max} \cdot \tanh\{2\zeta t/\tau_p\} & 0 \leq t < \tau_p/2 \\ v_{1\max} \cdot \tanh\{2\zeta(1 - t/\tau_p)\} & \tau_p/2 \leq t < \tau_p \end{cases} \quad (1)$$

In the frequency-modulated frame [62], the instantaneous frequency offset is equal to

$$\Delta v_0(t) = \Delta v_{0\max} \frac{\tan\{\kappa(1 - 2t/\tau_p)\}}{\tan(\kappa)} \quad (2)$$

where $v_{1\max}$ is the peak rf-amplitude, $\Delta v_{0\max}$ the peak rf-frequency modulation and ζ and κ are two adjustable parameters that are used to smoothen the effective field at both pulse edges. In the absence of CSA and for on-resonance irradiation, i.e. the carrier frequency in the center of the pulse is equal to the resonance frequency, the quality factor in the first adiabatic frame is given by [59]

$$Q_1 = \frac{v_{1\max}^2}{v_R \Delta v_{0\max}} \frac{\pi \tan(\theta)}{\theta} \tanh^2(\zeta) . \quad (3)$$

Furthermore, for solids exhibiting inhomogeneous broadening, the maximum of the echo signal in a spin-echo experiment decays for increasing τ delay with a time constant T_2' , which is much longer than the time constant, T_2^* , of the free induction decay (FID). Therefore, the refocused echo can be acquired during the second τ delay, which can improve the S/N ratio by a factor of up to $\sqrt{2}$.

III Theory

III.1 S/N ratio with UDEFT

The analytical expression of the DEFT signal has been derived in the steady-state regime [52]. However, this expression does not allow calculating the sensitivity enhancement provided by UDEFT when only a few scans are acquired or when the initial longitudinal magnetization (M_0) differs from that at thermal equilibrium (M_∞), e.g. when using DNP. Therefore, we derive below a more general expression (i) valid for any arbitrary initial longitudinal magnetization, and (ii) taking into account the contribution of the transient regime. The signal of UDEFT is calculated as a function of the number of scans (NS) for a given total experimental time, T_{exp} . We assume that (i) the longitudinal magnetization relaxes towards M_∞ during the relaxation delay, τ_{RD} , according to an exponential with T_1 constant-time, (ii) $2\tau \ll T_1$ and τ_{RD} , and (iii) the longitudinal relaxation during the τ delays can be disregarded.

The total experimental time can be expressed in T_1 unit as $T_{\text{exp}} = AT_1 \approx NS \cdot \tau_{\text{RD}}$, which allows defining the dimensionless parameter, Ψ , as:

$$\Psi = \tau_{\text{RD}}/T_1 \approx A/NS \quad (4)$$

The efficiency, E , of the UDEFT sequence is defined as the fraction of the longitudinal magnetization before the first $\pi/2$ -pulse, which is returned back to the z-axis after the second π -pulse. Given the above assumption, E can be expressed as

$$E = E_{\text{rf}} \cdot e^{(-2\tau/T_2')} \quad (5)$$

For ideal pulses, $E_{\text{rf}} = 1$, and the total magnetization is returned back to the z-axis by the UDEFT sequence. The $e^{(-2\tau/T_2')}$ term represents the attenuation due to transverse relaxation.

Assuming that random fluctuations dominate the electronic noise, we show in the SI (Supporting Information) that the S/N ratio of UDEFT experiment, for which only the first FID is recorded, can be written as

$$\frac{S^{UDEFT}}{N}(NS) = K \left(\frac{e^{-\psi}}{\sqrt{NS}} \left\{ M_0 - \frac{E \cdot M_\infty (1 - e^{-\psi})}{1 - E \cdot e^{-\psi}} \right\} \frac{1 - (E e^{-\psi})^{NS}}{1 - E \cdot e^{-\psi}} + \sqrt{NS} \frac{M_\infty (1 - e^{-\psi})}{1 - E \cdot e^{-\psi}} \right) \quad (6)$$

where K is a constant depending on factors, such as the coil geometry, its filling factor, its temperature, its resistance, the Larmor frequency and the signal apodization [65]. As seen in Eq.6, the S/N ratio is the sum of two terms corresponding to the contributions of the transient (1st) and steady-state (2nd) regimes, respectively. As seen in Fig.S1, the transient regime only significantly contributes to the S/N ratio in the case of (i) short experimental time, i.e. $A = T_{\text{exp}}/T_1 \approx NS \cdot \tau_{\text{RD}}/T_1$ is small (Fig.S1a,b) or (ii) hyperpolarized experiments for which M_0 is much larger than M_∞ (Fig.S1d). Furthermore, when the initial magnetization is small, the FIDs acquired during the transient regime mainly contain noise and decrease the S/N ratio (Fig.S1a).

III.2 S/N ratio with SP

For a SP experiment with a flip angle θ , we show in the SI that the S/N is given by

$$\frac{S^{SP}}{N}(NS) = K \cdot \sin(\theta) \left[\frac{e^{-\psi}}{\sqrt{NS}} \left\{ M_0 - \frac{\cos(\theta) \cdot M_\infty (1 - e^{-\psi})}{1 - \cos(\theta) \cdot e^{-\psi}} \right\} \frac{1 - (\cos(\theta) \cdot e^{-\psi})^{NS}}{1 - \cos(\theta) \cdot e^{-\psi}} + \sqrt{NS} \frac{M_\infty (1 - e^{-\psi})}{1 - \cos(\theta) \cdot e^{-\psi}} \right] \quad (7)$$

III.3 Comparison of UDEFT and SP sensitivities

Fig.2 shows the plot of the S/N of UDEFT and SP experiments versus NS and either E for UDEFT or θ for SP for $A = 5$ (Fig.2a,b) or 25 (Fig.2c,d). It must be noted that the S/N of UDEFT shown in Fig.2b,d is obtained when *only the first FID* is acquired for each scan. The acquisition of the refocused echo can increase the S/N ratio by a factor of up to $\sqrt{2}$, but this gain depends on E .

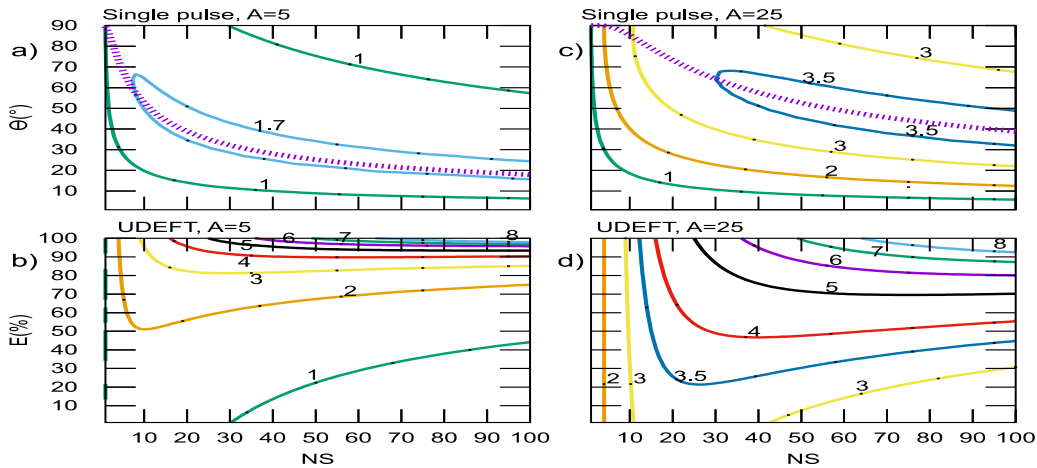


Fig.2. Plot of S/N of (a,c) SP and (b,d) UDEFT experiments lasting $T_{\text{exp}} = 5T_1$ (a,b) or $25T_1$ (c,d) versus NS and either θ (°) for SP or E (%) for UDEFT. For each scan of UDEFT, only the 1st FID has been acquired. The S/N ratio was calculated from Eqs. 6 and 7. We assumed $K = M_0 = M_\infty = 1$. (a,c) We also show the curve corresponding to the Ernst angle as a thick dashed purple line (Eq.8).

As expected, the S/N ratio increases with T_{exp} and is higher in Fig.2c and 2d than in 2a and 2b. As seen in Figs.2a and 2c, the maximal S/N ratio for a SP experiment is achieved for a flip angle corresponding to the Ernst angle [66]:

$$\theta_E = \arccos[e^{-\psi}] \quad (8)$$

For small NS , the Ernst angle curves deviate from optimum conditions because of the transient contribution.

For UDEFT experiments (Figs. 2b and 2d), the S/N ratio increases with E . For a given E value, the optimal number of scans, NS_{opt} , yielding the optimal ratio, $(S/N)_{\text{opt}}$, increases with T_{exp} (Table 1). For both $T_{\text{exp}} = 5T_1$ and $25T_1$, the UDEFT experiments yield higher $(S/N)_{\text{opt}}$ than SP ones. The gain in S/N ratio for UDEFT with respect to SP increases with E . For a given E value, the gains are similar for both $T_{\text{exp}} = 5T_1$ and $25T_1$. As example, for $E = 70\%$, UDEFT yields a 40% enhancement in S/N , which allows a two-fold reduction in T_{exp} .

Table.1. NS_{opt} and $(S/N)_{\text{opt}}$ for SP and UDEFT experiments with $T_{\text{exp}} = 5T_1$ or $25T_1$. The S/N ratios were calculated from Eqs.6 and 7 with $K = M_0 = M_{\infty} = 1$. For UDEFT experiment, only the 1st FID was acquired. For ideal pulses, $E = 70, 90$ and 95% correspond to $T_2'/\tau = 5.6, 19$ and 39 , respectively. These ratios are commonly encountered for non-protonated disordered samples [33,36].

T_{exp}	Scheme	NS_{opt}	$(S/N)_{\text{opt}}$	Gain in S/N
$5T_1$	SP ($\theta = 65\text{-}15^\circ$)	10-100	1.7	1
	UDEFT ($E = 70\%$)	17	2.4	1.4
	90 %	60	4.0	2.3
	95 %	100	5.6	3.2
$25T_1$	SP ($\theta = 65\text{-}35^\circ$)	40-100	3.6	1
	UDEFT ($E = 70\%$)	80	5	1.4
	90 %	250	8.3	2.3
	95 %	500	11.5	3.2

III.4 Quantitative measurements

Quantitative measurements require the longitudinal magnetization after n scans, $M_{R,n}$, to be close to M_{∞} for most of the scans. Hence, in the steady-state regime, we must have

$$M_{R,n} = M_{R,n-1} = mM_{\infty} \quad (9)$$

with m very close to 1. We show in Section I-3 of SI that this condition is met for UDEFT when the relaxation delay is given by

$$\tau_{\text{RD,min}} \geq T_{1,\text{max}} \cdot \ln \left(\frac{1-m \cdot E}{1-m} \right) \quad (10)$$

with $T_{1,\text{max}}$ the longest T_1 value of the different sites of the sample and

$$\tau_{\text{RD,min}} \geq T_{1,\text{max}} \cdot \ln \left(\frac{1-m \cdot \cos(\theta)}{1-m} \right) \quad (11)$$

for SP. These minimal relaxation delays and Eqs. 6 and 7 yield the maximal S/N ratios of

$$S/N(E, T_1) \leq K \frac{m \cdot M_{\infty}}{\sqrt{\tau_{\text{RD,min}}}} = KmM_{\infty} / \sqrt{T_{1,\text{max}} \cdot \ln \left(\frac{1-m \cdot E}{1-m} \right)} \quad (12)$$

for quantitative UDEFT experiments and

$$S/N(\theta, T_1) \leq K \frac{m \cdot M_{\infty} \cdot \sin(\theta)}{\sqrt{\tau_{\text{RD,min}}}} = KmM_{\infty} \sin(\theta) / \sqrt{T_{1,\text{max}} \cdot \ln \left(\frac{1-m \cdot \cos(\theta)}{1-m} \right)} \quad (13)$$

for quantitative SP ones.

As seen in Fig. 3a, quantitative SP spectra can be acquired using $\pi/2$ -pulse provided $\tau_{\text{RD,min}} \approx 4.5T_{1,\text{max}}$. Smaller flip-angles allow the use of shorter τ_{RD} delays. For example, $\tau_{\text{RD,min}} = 2.5T_{1,\text{max}}$ for $\theta = 30^\circ$. Hence, to acquire quantitative SP spectra of unknown samples, it is preferable to use small θ angles. For UDEFT, $\tau_{\text{RD,min}}$ decreases inversely to E , and for instance, $E \geq 87\%$ is required to record quantitative UDEFT spectra with $\tau_{\text{RD,min}} = 2.5T_{1,\text{max}}$.

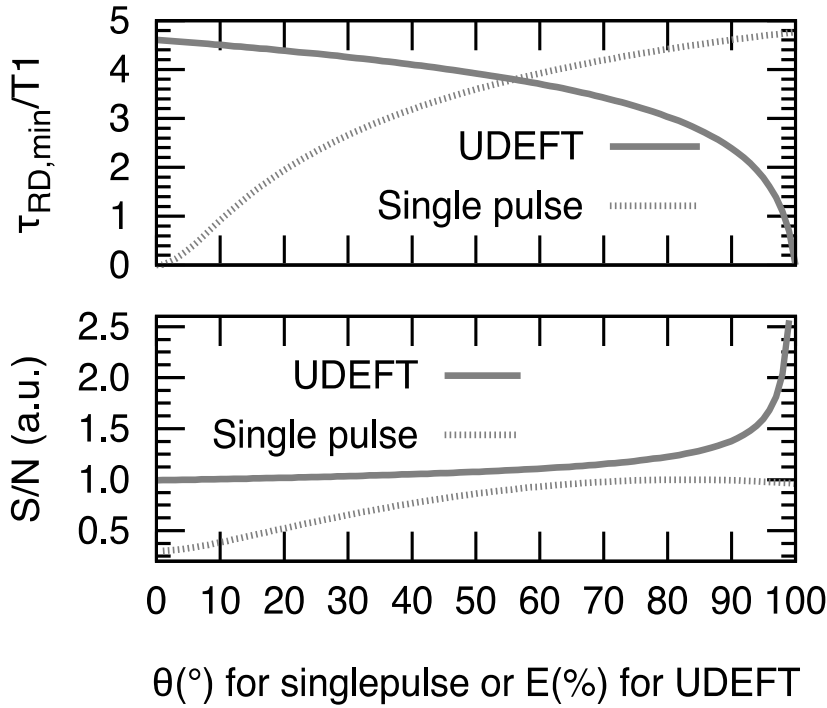


Fig.3. Plots of (a) $\tau_{RD,min}/T_{1,max}$ ratios (Eqs.10,11) and (b) maximal S/N ratios (Eqs.12,13) for quantitative SP and UDEFT measurements with $m = 0,99$ versus θ (°) for SP (dashed line) or E (%) for UDEFT (continuous line).

Fig.3b shows that the maximal S/N ratio for quantitative SP experiments is achieved for $\theta \approx 85^\circ$, whereas the use of $\theta = 30^\circ$ results in a 35 % decrease. Conversely, the S/N of UDEFT experiment monotonously increases with E . The sensitivity of quantitative UDEFT experiments with $E = 87\%$ is 31 % higher than that of quantitative SP ones.

IV Numerical simulations

IV.1 Simulation parameters

All spin dynamics simulations were performed using the SIMPSON software [67]. The powder averaging was calculated using 1344 $\{\alpha_{PR}, \beta_{PR}, \gamma_{PR}\}$ Euler angles describing the orientation of the principal axes of the ^{29}Si chemical shift tensor in the rotor frame. The 168 $\{\alpha_{PR}, \beta_{PR}\}$ Euler angles were selected according to the REPULSION algorithm [68], while the 8 γ_{PR} angles were regularly stepped from 0 to 360° .

Simulations were carried out for an isolated ^{29}Si nucleus to test the robustness of UDEFT to rf-inhomogeneity, offset and CSA using composite and adiabatic π -pulses as refocusing and inversion elements. For those simulations, the starting and detection operators were I_z . The static magnetic field was fixed at 9.4 T with $\nu_R = 4$ (Tables S1-3, Figs.S2,S3) or 10 kHz (Figs.4,S4,S6).

For all simulations, τ delays were approximately equal to 2 ms and were chosen in such way that there was a multiple number of rotor periods between the centers of the $\pi/2$ -pulses and that of the refocusing one. In Tables S1 and S2 as well as Fig.S2, we used ideal $\pi/2$ -pulses. In Table S1 and Fig.S2a, the inversion π -pulse was also ideal and in Table S2 and Fig.S2b, an ideal refocusing π -pulse was used. The lengths of the pulses, which are not ideal, were calculated for a nominal rf-field $\nu_{1nom} = 70$ kHz in Tables S1 to S3 and Figs.S2,S3 and $\nu_{1nom} = 50$ kHz in Figs.4,S4,S6.

The isotropic chemical shifts of ^{29}Si nuclei extend from -200 to 60 ppm, which corresponds to a maximal offset of 10 kHz at $B_0 = 9.4$ T [69,70]. For Si atoms forming single covalent bonds, the CSA

ranges from -60 to 90 ppm and hence, can reach 7 kHz at $B_0 = 9.4$ T [71–74]. For Si atoms forming multiple bonds, the CSA can reach -640 ppm, i.e. 50 kHz at $B_0 = 9.4$ T [6,75,76]. The rf-field produced by a solenoid coil is highly inhomogeneous [77–79], and for a 4 mm rotor it has been shown that the rf-field at the ends of the rotor, $v_{1\text{edge}}$, is approximately 20% of its maximal value at the center of the coil, $v_{1\text{center}}$ [77]. The robustness to rf-inhomogeneity (Tables S1–3) was investigated by varying the rf-field from 40 to 100 kHz for the refocusing and/or inversion pulses.

In Figs. 4, S4, we also compared the robustness of UDEFT using as refocusing element: either a single π -pulse, denoted $P180_x$, or $59_{180}298_{059_{180}}$ or $58_{0140_{180}344_{0140_{180}58_0}}$ composite- π pulses, called CP_{x1} and CP_{x2} , and as inversion element: either a single π -pulse, called $P180_z$, or $90_{0240_{90}90_0}$ or $90_{90}180_{090_{90}}$ composite π -pulses, called CP_{z1} and CP_{z2} . We also used the adiabatic tanh/tan inversion pulse, called AP_z , which lasted $\tau_p = 50$ μs and used $\Delta v_{0\text{max}} = 1.5$ MHz with $\zeta = 10$ and $\kappa = \text{atan}(30) = 88^\circ$. It must be noted that $\tau_p = 25$ and 100 μs gave similar results for AP_z (not shown). The Simpson files used for Figs. 4, S4 are provided in the SI. To quantify this robustness, we have calculated the E_{rf} efficiency for offset values ranging from -30 to 30 kHz and rf-fields ranging from 35 to 75 kHz, for CSA = 2 (Fig. 4) and 20 kHz (Fig. S4).

IV.2 Robustness of UDEFT to rf-field, offset and CSA

In order to improve the robustness of UDEFT to rf-field, offset and CSA, we tested seven refocusing composite π -pulses listed in Table S1, the other pulses being ideal. These pulses have a total flip angle $\theta_{\text{tot}} \leq 900^\circ$ and hence, for $v_{1\text{nom}} = 70$ kHz, their lengths did not exceed 35 μs , a duration much shorter than the rotor period: $T_R = 250$ μs . We tested composite π -pulses with variable or quasi-constant rotation axis designed to compensate either the rf-inhomogeneity or the offset. For constant rotation composite- π -pulses, the rotation axis remains approximately along the x axis across their effective rf-field and offset bandwidths [55,80–82]. These pulses have been shown to be better-suited than variable rotation ones for refocusing purpose in spin-echo experiments [83]. Table S1 shows that when used as refocusing elements, the constant rotation pulses designed to invert the longitudinal magnetization with offset compensation [82], CP_{x1} and CP_{x2} , significantly improve the robustness of UDEFT to offset with respect to $P180_x$ without deteriorating the robustness to rf-inhomogeneity. Moreover, CP_{x2} better compensates for offset than CP_{x1} . The other tested pulses do not improve the robustness of UDEFT, or even lower it. Furthermore, Fig. S2a shows that CP_{x1} and CP_{x2} improve the robustness to CSA with respect to $P180_x$. Composite tanh/tan adiabatic pulses, including BIR-4 [61,62] and three successive adiabatic pulses with relative lengths of $\tau_p/4$, $\tau_p/2$ and $\tau_p/4$ [56], were also tested as refocusing element in UDEFT. However, they were less efficient and robust, notably to CSA, than CP_{x1} and CP_{x2} . Antisymmetric composite π -pulses have been shown to act as efficient and robust refocusing elements in spin-echo experiments [84,85]. However, we have analyzed the use of these pulses with UDEFT and observed (not shown) that they are not robust to CSA owing to their very long lengths ($\theta_{\text{tot}} = 1620$ or 2340°).

We also tested six composite π -pulses listed in Table S2 as inversion elements in UDEFT, the other pulses being ideal. The variable rotation pulses, CP_{z1} and CP_{z2} , have been designed to invert the longitudinal magnetization with compensation of both rf-inhomogeneity and offset for CP_{z1} and only rf-inhomogeneity for CP_{z2} [54,86]. CP_{z1} yields a higher robustness to offset and CSA than CP_{z2} and $P180_z$ (Fig. S2b).

We also investigated the robustness to rf-field, offset and CSA of UDEFT built with the most robust refocusing (CP_{x1} and CP_{x2}) and inversion (CP_{z1} and CP_{z2}) composite elements. The robustness of these sequences made of two composite π -pulses was compared to that of sequences using one composite and one single π -pulses, or two single π -pulses. In this case, all pulses had a finite length. Table S3 indicates that the sequences with CP_{x1} - CP_{z1} and CP_{x2} - CP_{z1} pairs of composite π -pulses are the most robust to both rf-inhomogeneity and offset. The combination CP_{x2} - CP_{z1} is more robust to offset than CP_{x1} - CP_{z1} , but this is the contrary with respect to CSA (Fig. S3).

Adiabatic tanh/tan pulse, AP_z , was also employed as inversion element. For a CSA of 2 kHz, Fig. 4 shows that AP_z leads to a better robustness to rf-inhomogeneity than CP_{z1} and CP_{z2} , and that it can be

combined with CP_{x1} or CP_{x2} refocusing pulses in order to further improve the robustness to offset. As seen in Fig. S4, a larger CSA decreases the efficiency of UDEFT. Such decrease is more pronounced when AP_z is combined with CP_{x2} than with CP_{x1} , since CP_{x1} is more robust to CSA than CP_{x2} (Fig. S3). Given the typical offset and CSA values for ^{29}Si nuclei at $B_0 = 9.4$ T ($\Delta\nu_{\text{offset}} \leq 10$ kHz and $\text{CSA} \leq 7$ kHz for ^{29}Si nuclei forming single covalent bonds) and the typical rf-inhomogeneity of MAS probes ($\nu_{\text{edge}}/\nu_{\text{center}} = 20\%$), UDEFT scheme using CP_{x1} and AP_z as refocusing and inversion pulses is the most robust sequence at such magnetic field.

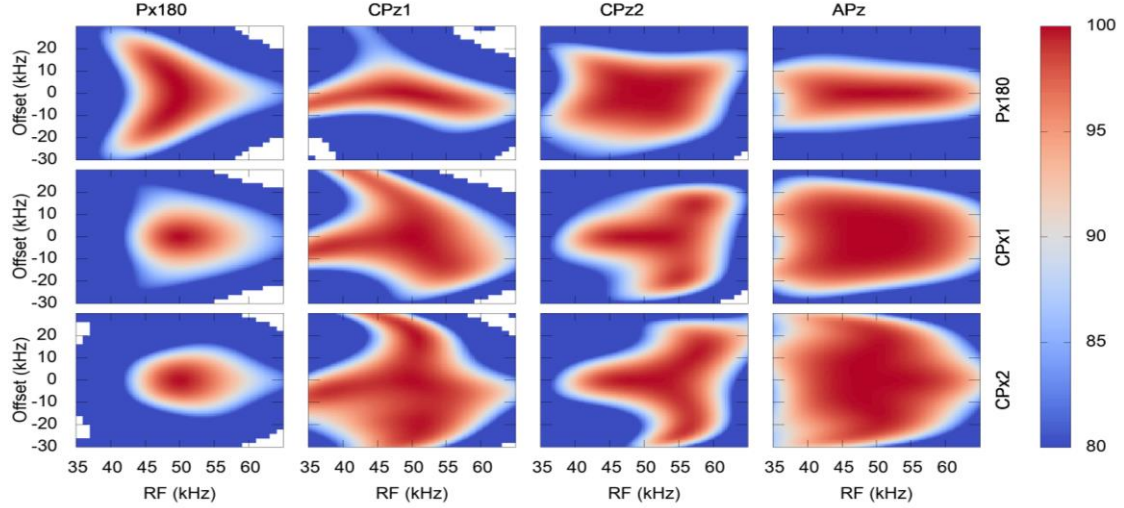


Fig. 4. Simulated E_{rf} efficiency versus rf-field and offset for UDEFT schemes using the refocusing and inversion pulses indicated on the right and the top of the figure, respectively. Simulations were performed for ^{29}Si CSA of 2 kHz, i.e. 25 ppm at $B_0 = 9.4$ T with $\nu_{\text{1nom}} = 50$ kHz and $\nu_R = 10$ kHz. In these simulations, all pulses have finite lengths. The plotted E_{rf} efficiency corresponds to the geometric average of two successive scans, for which the phases of refocusing and inversion pulses are incremented by 180° (caption of Fig. 1 and Section IV.3). For instance, for UDEFT scheme with $P180_x$ and $P180_z$, the 1st and 2nd scans correspond to $90_{90^\circ}\text{-}\tau\text{-}180_{180^\circ}\text{-}\tau\text{-}90_{90^\circ}\text{-}180_{180^\circ}$ and $90_{90^\circ}\text{-}\tau\text{-}180_{180^\circ}\text{-}\tau\text{-}90_{90^\circ}\text{-}180_{180^\circ}$ sequences and the plotted efficiency is equal to $E_{\text{rf}} = [E_{\text{rf}}(1^{\text{st}} \text{ scan}) \cdot E_{\text{rf}}(2^{\text{nd}} \text{ scan})]^{1/2}$.

IV.3 Stimulated echoes and phase cycling

Fig. S5 displays some of the possible coherence transfer pathways during UDEFT experiments. The desired coherence transfer-pathways (Fig. S5a): (i) correspond to changes in coherence order of $\Delta p = \pm 2$ by each refocusing pulse, and (ii) they produce FIDs which are maximal at the beginning of the odd τ delays and at the end of the even ones. With actual refocusing pulses, changes of $p = \pm 1$, called stimulated echoes, are detected, which are maximal at the end of the odd τ delays and at the beginning of the even ones (Figs. S5b and c). The truncation of these stimulated echoes leads to undesirable oscillations around the base of the peaks. The contribution of some of these stimulated echoes to the UDEFT signal can be removed by incrementing by 180° the phase of the refocusing pulse, while the phase of the receiver remains constant. However, some of the stimulated echoes are refocused after the τ_{RD} delay, which is often much shorter than T_1 . These echoes cannot be removed by the two-phase cycling and they produce artifacts. Stimulated echoes corresponding to $\Delta p = 0$ by the refocusing pulse do not produce artifacts in the UDEFT spectrum (Figs. S5d and e). Furthermore, an imperfect inversion pulse can result in a residual magnetization pointing toward the $-\hat{z}$ direction during τ_{RD} , which reduces the UDEFT signal.

Fig. S6 displays the simulated E_{rf} efficiency for various coherence pathways of the $CP_{x1}\text{-}AP_z$ sequence. These simulations show that incrementing the phase of the refocusing pulse by 180° (i) does not modify the signal intensity for the desired pathway corresponding to $\Delta p = \pm 2$, but (ii) inverts the sign of the signal corresponding to $\Delta p = \pm 1$, hence eliminating these stimulated echoes. They also show that incrementing simultaneously the phase of the refocusing π -pulse by 90° and that of the second $\pi/2$ -pulse and the receiver by 180° allows removing the undesired coherence transfer pathways corresponding to $\Delta p = 0$ during the refocusing pulse. However, as explained above, these pathways do

not produce artifacts. Hence, a two-step phase cycle, in which the phase of the refocusing pulse is incremented by 180° , is sufficient. Furthermore, simulations [not shown] indicate that the E_{rf} efficiency depends on the relative phase of the refocusing and inversion pulses, except in the case of adiabatic inversion pulse. Therefore, the phase of the inversion pulses is incremented simultaneously with that of the refocusing pulse, as described in the caption of Fig. 1.

V Experimental results

V.1 Experimental conditions

NMR experiments were carried with five different samples: 98% ^{29}Si -enriched (i) amorphous silica, and (ii) borosilicate glass with $8\text{Na}_2\text{O}-31\text{B}_2\text{O}_3-61\text{SiO}_2$ molar composition prepared as described in ref. [87], or unlabeled (iii) SBA-15 mesoporous silica with a BET surface area of $650\text{ m}^2\cdot\text{g}^{-1}$ and an average pore diameter determined by BJH adsorption of 5.4 nm, (iv) mesoporous silica nanoparticles (MSNs) functionalized with 3-(N-phenylureido)propyl (PUP) groups synthesized as described in ref. [88], and (v) flame retardant material used in fire protection of steel building structures. This last material was obtained by the thermal treatment of a mixture of 92% mol of a silicone resin and 8% mol of a modifier, which is itself a mixture of polydimethylsiloxane and silica coated by a silane [89].

All experiments were acquired on a wide-bore 9.4 T Bruker NMR spectrometer equipped with an Avance-II console and a $\varnothing = 4\text{ mm}$ double resonance HX MAS probe, except in Fig. 9 ($\varnothing = 7\text{ mm}$). The rotors were fully packed with the sample, except in Fig. 6, and spun at $\nu_R = 10\text{ kHz}$, except in Fig. 9 ($\nu_R = 5\text{ kHz}$). The T_1 and T_2' time constants were measured using saturation recovery and spin-echo experiments, respectively. ^{29}Si 1D UDEFT spectra were recorded for all samples, CPMG ones for SBA-15 and MSNs, and SP ones for SBA-15 and flame retardant material. For UDEFT experiments, the delays between the middles of the $\pi/2$ -pulses and that of the refocusing π -pulse were rotor-synchronized, i.e. equal to a multiple of the rotor period, except in Fig. 5. Similarly, the delays between the middles of the π -pulses in CPMG experiments were also rotor-synchronized. For UDEFT scheme using AP_z , the adiabatic \tanh/\tan inversion pulse lasted $\tau_p = 50\text{ }\mu\text{s}$ with $\zeta = 10$ and $\kappa = \arctan(30) = 88^\circ$. No ^1H decoupling was applied, except in Figs. 8 and 9. The ^{29}Si isotropic chemical shift was referenced to neat TMS. The other experimental parameters are given in the figure captions.

V.2 Rotor synchronization of UDEFT

We first recorded the ^{29}Si 1D UDEFT spectrum of ^{29}Si -enriched amorphous silica, which contains approximately 90 and 10 % of Q^4 and Q^3 sites, respectively. We measured $T_1 \approx 55\text{ s}$, $T_2' \approx 13\text{ ms}$ and a global efficiency for UDEFT sequence of $E = 75\%$. The $^2J_{\text{Si-O-Si}}$ coupling constants are typically smaller than 25 Hz [32,90], and hence the coherent signal decay produced by these J -couplings during a spin-echo is below 5% with $\tau \approx 2\text{ ms}$. This decay is taken into account in the T_2' value. These J -couplings lead to the creation of antiphase single-quantum coherences, but their lifetime being much shorter than τ_{RD} , they do not contribute to the detected signal. As seen in Fig. 5, the intensity of UDEFT experiments is maximum when the $\pi/2$ -pulses and the refocusing π -pulse are rotor-synchronized. When it is not the case, ^{29}Si CSA and ^{29}Si - ^{29}Si dipolar anisotropic interactions are reintroduced and decrease the signal intensity.

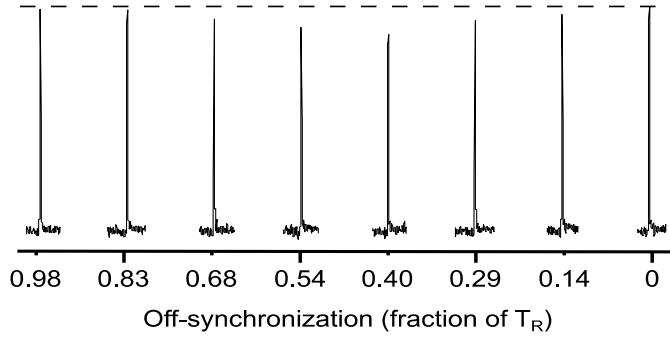


Fig.5. Experimental ^{29}Si UDEFT $\text{P180}_x\text{-P180}_z$ signal of ^{29}Si -enriched amorphous silica sample versus the deviation between the delays between the 90° pulses and the refocusing pulse and a multiple of the rotor period. The horizontal dashed line facilitates the comparison of the signal intensity. $B_0 = 9.4\text{ T}$, $\nu_R = 10\text{ kHz}$, $\nu_1 = 75\text{ kHz}$, $\tau = 2\text{ ms}$, $\text{NS} = 16$, $\tau_{\text{RD}} = 1\text{ s}$.

V.3 Robustness to rf-field and offset of UDEFT

To test the robustness to rf-inhomogeneity, we recorded UDEFT spectra of amorphous silica using $\text{P180}_x\text{-P180}_z$, $\text{CP}_{x1}\text{-AP}_z$ and $\text{CP}_{x1}\text{-CP}_{z1}$ pairs of elements, versus the rf-field of the various pulses varied independently. Fig. **S7** show that for the inverting element, AP_z is significantly more robust than P180_z and CP_{z1} , whereas for the refocusing element, P180_x and CP_{x1} exhibit similar robustness in agreement with simulation results in Table **S1**.

In order to compare the robustness to rf-inhomogeneity and offset of UDEFT schemes using different refocusing and inversion pulses, we also recorded spectra of a borosilicate glass for various rf-field and offset values (Fig. **6**). To increase the rf-homogeneity, the sample was restricted to a slice at the center of the rotor. It must be noted that the signal which would be observed for slices at other locations where the rf-field is equal to ν_1 , is equal to that shown in Fig. **6b** scaled by $\nu_1/\nu_{1,\text{nom}}$. Indeed, according to the reciprocity principle, the induced voltage in the coil is proportional to the rf-field [78]. In a full rotor sample, the signal would then be the integrated intensity of these curves.

This glass mostly contains Q^3 and Q^4 sites with $T_1 \approx 400\text{ s}$ and $T_2' \approx 10\text{ ms}$. For on-resonance pulses using nominal rf-field, the global UDEFT efficiency is approximately equal to 70% for $\tau = 1.5\text{ ms}$. UDEFT schemes with either $\text{CP}_{x1}\text{-AP}_z$ or $\text{CP}_{x1}\text{-CP}_{z1}$ exhibit similar robustness to offset but are more robust than with $\text{P180}_x\text{-P180}_z$ (Fig. **6a**). The results shown in Fig. **6b** are consistent with the simulations of Fig. **S6** and they show that UDEFT with $\text{CP}_{x1}\text{-AP}_z$ is more robust to rf-field than that with $\text{CP}_{x1}\text{-CP}_{z1}$, which is itself more robust than with $\text{P180}_x\text{-P180}_z$.

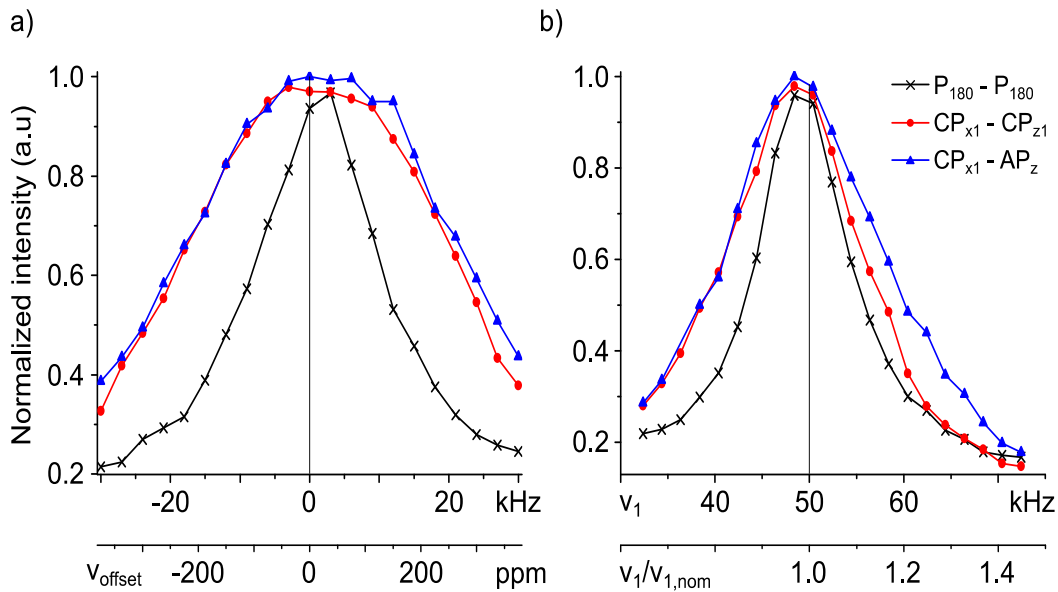


Fig.6. Experimental ^{29}Si UDEFT signal of ^{29}Si -enriched borosilicate glass versus (a) offset in kHz (top) and ppm at 9.4 T (bottom), and (b) rf-field in kHz (top) and relative value with respect to $v_{1\text{nom}} = 50$ kHz (bottom) for schemes using: P180_x-180_z (x), CP_{x1}-CP_{z1} (•), and CP_{x1}-AP_z (▲). $B_0 = 9.4$ T, $v_R = 10$ kHz, $\tau = 1.5$ ms, NS = 32, $\tau_{RD} = 5$ s. To ensure identical initial magnetization, experiments started by a pre-saturation train of pulses followed with a delay of 900 s. The lengths of the single and composite pulses were calculated using $v_{1\text{nom}}$. For AP_z, $\tau_p = 50$ μs and $\Delta v_{0,\text{max}} = 1.5$ MHz. In (b), the pulses were applied on-resonance with the Q⁴ signal.

V.4 Comparison of UDEFT, SP and CPMG sensitivities

The sensitivities of UDEFT, SP and CPMG experiments were compared on SBA-15, which mainly contains Q³ and Q⁴ sites. The build-up curves of the ^{29}Si longitudinal magnetization of Q⁴ sites can be modeled as a stretched exponential with $\beta = 0.52$ and $T_1 = 394$ s (Fig. S8), which means that these sites exhibit a distribution of T_1 constant. Similarly, the decay of Q⁴ signal in a spin-echo experiment is bi-exponential with $T'_{2f} = 0.34$ s and $T'_{2s} = 1.34$ s for the fast and slow components (Fig. S9). The distribution of T_1 and T_2' values may stem from a faster longitudinal and transverse relaxation of Q⁴ sites located near the surface than in the core of the silica wall.

We first compared the sensitivities of UDEFT variants using as π -pulse pairs: CP_{x1}-AP_z, CP_{x1}-CP_{z1} and P180_x-P180_z. When using CP_{x1}-AP_z, we first optimized the number of scans (NS) to acquire the spectrum within an experimental time of $T_{\text{exp}} = 1$ h (Fig. 7a). The same parameters were used to acquire the spectra of Figs. 7b and c for CP_{x1}-CP_{z1}, and P180_x-P180_z, respectively. The sequence using CP_{x1}-AP_z yields higher signal than the other variants. This result is consistent with the higher robustness of this sequence to rf-inhomogeneity (Sections IV.2 and V.3). Furthermore, spectra of Figs. 7b and c exhibit more intense wiggles. These truncation artifacts stem from undesirable stimulated echoes, as seen in Fig. S10. Indeed, P180_z and CP_{z1} are less robust to rf-inhomogeneity than AP_z, thus producing (i) an imperfect inversion in regions of the sample where the rf-field deviates from its nominal value, and hence (ii) more intense stimulated echoes. These experimental results confirm that UDEFT with CP_{x1}-AP_z has to be preferred. Furthermore, the acquisition of the refocused FID during the second τ delay of UDEFT experiment allows enhancing the sensitivity by $\sqrt{2}$, as seen in Fig. 7e. This gain corresponds to the theoretical limit since this sample features long T_2' values and the losses during 2τ are limited. We then compared these spectra with those obtained with SP and CPMG. For SP experiment, the pulse length and the number of scans were optimized to maximize the sensitivity, which provided the spectrum shown in Fig. 7d. Its sensitivity is approximately 9-fold lower than that of the best UDEFT version (Fig. 7e). Conversely, for that sample featuring very long T_2' values, the sensitivity of CPMG experiment is 70% higher than that of UDEFT (compare Figs. 7e and f).

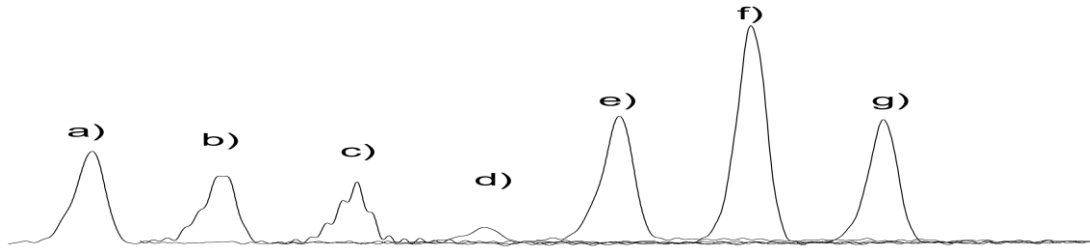


Fig.7. ^{29}Si MAS spectra of SBA-15 acquired using (a-c, e) UDEFT, (d) SP and (f,g) CPMG experiments. $B_0 = 9.4$ T, $v_R = 10$ kHz, $\tau = 2.7$ ms, $T_{\text{exp}} = 1$ h. To ensure identical initial magnetization, experiments started by a pre-saturation train of pulses followed with a 1 h delay. **UDEFT:** NS = 2048, $\tau_{RD} = 1.75$ s, with (a-c) only the 1st or (e) also the 2nd FID. (a,e) CP_{x1}-AP_z, (b) CP_{x1}-CP_{z1}, (c) P180_x-P180_z. AP_z: $\tau_p = 50$ μs , $v_{1,\text{max}} = 52$ kHz, $\Delta v_{0,\text{max}} = 2.5$ MHz. The rf-field of other pulses was 52 kHz. **SP:** $\tau_p = 2.1$ μs (flip-angle = 40°), $v_1 = 46$ kHz, NS = 128, $\tau_{RD} = 28$ s. **CPMG:** $v_1 = 52$ kHz, NS = 4, $n = 4096$ (f) or 256 (g). The intensities were carefully normalized to the same S/N ratio as in spectra (a-c) with NS = 2048: they were multiplied by $1/\sqrt{2}$ (e,f), 4 (d) and $2\sqrt{2}$ (g).

We also compared the sensitivity of UDEFT and CPMG experiments for the sample of MSNs functionalized with PUP groups. As seen in Fig. 8, the ^{29}Si spectrum of that sample exhibits three resolved resonance ascribed to T, Q³ and Q⁴ sites [91,92]. The concentration of protons in the pores is much higher for that sample than for SBA-15, and hence ^1H decoupling must be applied during the τ delays of UDEFT for resolution purpose and the full CPMG sequence to detect the refocused echoes. For UDEFT, the spin-echoes lasting 2τ are interleaved with τ_{RD} delays, during which no ^1H decoupling is

applied and the decoupling periods thus remain very short. For CPMG, the number of echoes acquired for each scan is limited by the power-handling specifications of the probe. For functionalized MSNs, only ten echoes could be acquired with CPMG so that the decoupling period does not exceed 50 ms. The comparison of the UDEFT and CPMG spectra shown in Fig. 8a indicates that UDEFT, for which only the 1st FID is acquired, is approximately 50 and 20 % more sensitive than CPMG for T and Q sites, respectively. UDEFT yields larger enhancement for the T sites than for the Q ones since the former are subject to larger ^1H - ^{29}Si dipolar couplings and their CPMG signal decays more rapidly. Furthermore, a 25% additional gain in sensitivity can be obtained by acquiring the 2nd FID with UDEFT. Hence, for these functionalized MSNs, UDEFT with acquisition of the two FIDs is approximately 80 and 50% more sensitive than CPMG for the detection of T and Q sites, respectively.

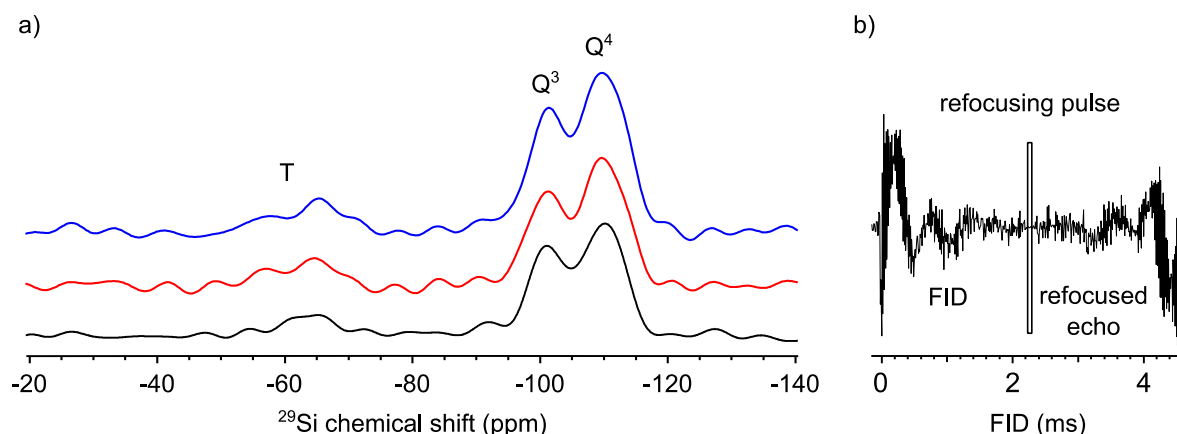


Fig. 8. (a) ^{29}Si MAS spectra of MSNs functionalized with PUP acquired with CPMG (bottom-black) or UDEFT $\text{CP}_{\text{x1}}\text{-AP}_2$ with either only the 1st (middle-red) or also the 2nd-FID (top-blue). The signal intensities are scaled to have the same noise. SPINAL-64 ^1H decoupling with an rf-field of 80 kHz was applied during the delays of $\tau = 2.2$ ms. $B_0 = 9.4$ T, $\nu_R = 10$ kHz, $T_{\text{exp}} = 7$ h, $\nu_1 = 92$ kHz (except AP_2). **CPMG:** NS = 262, $\tau_{\text{RD}} = 96$ s, 10 echoes (limited by 50 ms acquisition to save the probe from ^1H decoupling). **UDEFT:** NS = 2096, $\tau_{\text{RD}} = 12$ s. AP_2 : $\tau_p = 50$ μs , $\nu_{1\text{max}} = 58$ kHz, $\Delta\nu_{0\text{max}} = 4$ MHz. (b) FIDs of UDEFT experiments.

V.5 Quantitative spectra

We also compared the quantification of ^{29}Si signals for the flame retardant material. The ^{29}Si spectrum of this sample exhibits three signals at -22 , -70 and -78 ppm, which are attributed to D sites of polydimethylsiloxane and T^2 and T^3 sites of silicone polymer, respectively. A very weak Q^4 site at ca. -110 ppm is observed for long acquisition time. The T_1 times of D and T sites ranges from 40 to 70 s. The ^{29}Si polydimethylsiloxane D site signal at -22 ppm is narrow with a linewidth below 30 Hz, but it was broadened to 100 Hz by an exponential multiplication in Fig. 9. The ^1H signals of those molecules are also very narrow, which indicates their high mobility. These fast and isotropic motions of polydimethylsiloxane chains are confirmed by the lack of D signal in $^1\text{H} \rightarrow ^{29}\text{Si}$ CPMAS experiments, which indicates vanishing ^1H - ^{29}Si dipolar couplings. On the contrary, the T sites exhibit broad signals, which are visible in $^1\text{H} \rightarrow ^{29}\text{Si}$ CPMAS spectra. Hence, the silicone polymers are rigid.

Fig. 9 compares the ^{29}Si MAS spectra of this material acquired with SP experiments using $\tau_{\text{RD}} = 180$ s and with UDEFT using τ_{RD} from 12.5 to 150 s, with the same number of scans. The intensity of UDEFT signals reaches that of SP for $\tau_{\text{RD}} = 50$ s for the D site and $\tau_{\text{RD}} = 75$ s for the T site. This result confirms the higher sensitivity of UDEFT experiment with respect to SP. The employed $\varnothing = 7$ mm probe produces highly inhomogeneous rf-field and UDEFT would yield better sensitivity gain using 4 mm probe. Furthermore, with UDEFT the intensity of the T site keeps increasing for $\tau_{\text{RD}} \geq 75$ s and exceeds that of SP spectrum. This result indicates that UDEFT spectra acquired within a shorter experimental time than the SP ones yield better quantification of the various sites. A quantitative analysis of the proportions and S/Ns of the ^{29}Si MAS spectra of flame retardant material shown in Fig. 9. is given in Table S4.

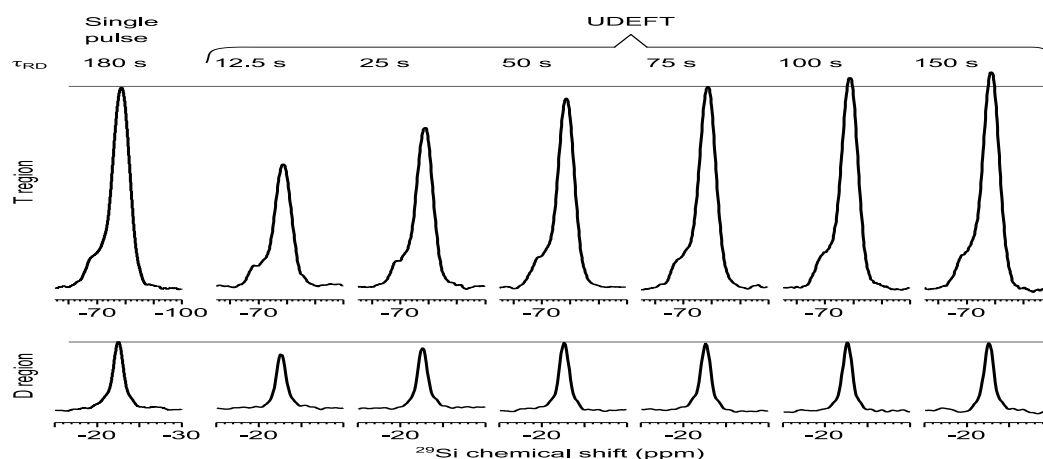


Fig.9. ^{29}Si MAS signals of D (bottom) and T (top) species of the flame retardant material acquired with SP (left) or UDEFT $\text{CP}_{\text{X1}}\text{-AP}_2$ (right) techniques. $B_0 = 9.4$ T, $\nu_R = 5$ kHz, $\text{NS} = 80$, $\nu_1 = \nu_{1,\text{max}} = 45$ kHz for all pulses of SP and UDEFT experiments. SPINAL-64 ^1H dipolar decoupling with rf-field of 40 kHz was applied during the 10 ms of FID (SP) or τ delays (UDEFT). **SP:** the FID was acquired after a $\pi/2$ -pulse. **UDEFT:** only the 1st FID was used to be quantitative. AP_2 : $\tau_p = 50$ μs , $\Delta\nu_{0\text{max}} = 3$ MHz. τ_{RD} delays are indicated above the spectra. The signal was multiplied by a decaying exponential function (Lorentzian broadening of 80 Hz) to remove residual truncation artifacts.

VI. Conclusions

We have demonstrated herein the possibility to acquire ^{29}Si MAS NMR spectra of solids using UDEFT experiment. We have shown that the use of $59_{180}298_{0}59_{180}$ refocusing composite π -pulse and adiabatic inversion pulse using tanh/tan modulation improves the efficiency of this sequence and its robustness to rf-inhomogeneity, offset and CSA. These pulses combined with the phase cycling limit the artifacts produced by stimulated echoes. We have theoretically and experimentally demonstrated the gain in sensitivity provided by UDEFT with respect to SP experiments for disordered samples with $T_2^* < T_2'$. The main limitation of UDEFT, and also CPMG, may be when the sample is very well crystallized with a small number of narrow resonances. Indeed, in this case the previous condition, $T_2^* < T_2'$, may not be met, which leads to very long delays and possible truncation effects. In the case of protonated samples, UDEFT experiment can also be more sensitive than CPMG since the power handling specification of the probe limits the maximal length of the ^1H decoupling and the number of echoes acquired during each scan of CPMG sequence. Furthermore, UDEFT sequence yields a better quantification of the NMR signals than SP, and a fortiori CPMG, while offering a higher sensitivity than quantitative SP experiments.

Using large rotor diameters (e.g. $\varnothing = 4$ or 7 mm) for UDEFT is useful for sensitivity reasons, especially in the case of unlabeled samples with very long relaxation times of several hundreds or thousands of seconds. However, for less demanding samples other options could be used, such as $\varnothing = 3.2$ mm rotors.

Acknowledgments. Chevreul Institute (FR 2638), Ministère de l'Enseignement Supérieur, de la Recherche et de l'Innovation, Region Hauts-de-France and FEDER are acknowledged for supporting and funding partially this work. Financial support from the IR-RMN-THC FR-3050 CNRS for conducting the research is gratefully acknowledged. Authors also thank contracts ANR-17-ERC2-0022 (EOS) and ANR-18-CE08-0015-01 (ThinGlass). This project has received funding from the European Union's Horizon 2020 research and innovation program under grant agreement No 731019 (EUSMI). OL acknowledge financial support from Institut Universitaire de France (IUF). Authors thank Jean-Sebastien Girardon from UCCS at the Lille-University for giving them the SBA-15 sample and Igor Slowing and Marek Pruski from Ames Laboratory (USA) for providing them the silica sample functionalized with 3-(N -phenylureido)propyl groups

In the SI, we provide: Figs.S1-S10, Tables S1-S3 and the SIMPSON input files for Figs.4 and S4. The pulse sequences for various Bruker consoles are provided in a separate archive.

- [1] M.A. Petrich, Amorphous Silicon Alloys, in: eMagRes, American Cancer Society, 2007. doi:10.1002/9780470034590.emrstm0010.
- [2] R.A. Faulkner, J.A. DiVerdi, Y. Yang, T. Kobayashi, G.E. Maciel, The Surface of Nanoparticle Silicon as Studied by Solid-State NMR, *Materials*. 6 (2013) 18–46. doi:10.3390/ma6010018.
- [3] D. Lee, G. Monin, N.T. Duong, I.Z. Lopez, M. Bardet, V. Mareau, L. Gonon, G. De Paëpe, Untangling the Condensation Network of Organosiloxanes on Nanoparticles using 2D ^{29}Si – ^{29}Si Solid-State NMR Enhanced by Dynamic Nuclear Polarization, *J Am Chem Soc.* 136 (2014) 13781–13788.
- [4] A.N. Thiessen, M. Ha, R.W. Hooper, H. Yu, A.O. Oliynyk, J.G.C. Veinot, V.K. Michaelis, Silicon Nanoparticles: Are They Crystalline from the Core to the Surface?, *Chem. Mater.* 31 (2019) 678–688. doi:10.1021/acs.chemmater.8b03074.
- [5] Y. Takeuchi, T. Takayama, ^{29}Si NMR Spectroscopy of Organosilicon Compounds, in: *Chem. Org. Silicon Compd.*, John Wiley & Sons, Ltd, 2003: pp. 267–354. doi:10.1002/0470857250.ch6.
- [6] V. Kravchenko, R. Kinjo, A. Sekiguchi, M. Ichinohe, R. West, Y.S. Balazs, A. Schmidt, M. Karni, Y. Apeloig, Solid-State ^{29}Si NMR Study of RSiSiR : A Tool for Analyzing the Nature of the Si–Si Bond, *J. Am. Chem. Soc.* 128 (2006) 14472–14473. doi:10.1021/ja065817s.
- [7] S. Kuroki, H. Kimura, I. Ando, Structural Characterization of Si-based Polymer Materials by Solid-State NMR Spectroscopy, in: *Annu. Rep. NMR Spectrosc.*, Academic Press, 2004: pp. 201–243. doi:10.1016/S0066-4103(04)52005-7.
- [8] J.D. Mackenzie, M.E. Smith, *Multinuclear Solid-state NMR of Inorganic Materials*, Pergamon, 2002.
- [9] S.J. Widgeon, S. Sen, G. Mera, E. Ionescu, R. Riedel, A. Navrotsky, ^{29}Si and ^{13}C Solid-State NMR Spectroscopic Study of Nanometer-Scale Structure and Mass Fractal Characteristics of Amorphous Polymer Derived Silicon Oxycarbide Ceramics, *Chem. Mater.* 22 (2010) 6221–6228. doi:10.1021/cm1021432.
- [10] B.L. Phillips, Crystallography and NMR: Applications to Geochemistry, in: eMagRes, American Cancer Society, 2009. doi:10.1002/9780470034590.emrstm1045.
- [11] K.T. Mueller, R.L. Sanders, N.M. Washton, Clay Minerals, in: eMagRes, American Cancer Society, 2014: pp. 13–28. doi:10.1002/9780470034590.emrstm1332.
- [12] S.E. Ashbrook, D.M. Dawson, NMR spectroscopy of minerals and allied materials, 45 (2016) 1–52. doi:10.1039/9781782624103-00001.
- [13] L. Mafra, J. Klinowski, Molecular Sieves: Crystalline Systems, in: eMagRes, John Wiley & Sons, Ltd, 2013. doi:10.1002/9780470034590.emrstm0315.
- [14] S. Smeets, Z.J. Berkson, D. Xie, S.I. Zones, W. Wan, X. Zou, M.-F. Hsieh, B.F. Chmelka, L.B. McCusker, C. Baerlocher, Well-Defined Silanols in the Structure of the Calcined High-Silica Zeolite SSZ-70: New Understanding of a Successful Catalytic Material, *J. Am. Chem. Soc.* 139 (2017) 16803–16812. doi:10.1021/jacs.7b08810.
- [15] R.P. Sangodkar, B.J. Smith, D. Gajan, A.J. Rossini, L.R. Roberts, G.P. Funkhouser, A. Lesage, L. Emsley, B.F. Chmelka, Influences of Dilute Organic Adsorbates on the Hydration of Low-Surface-Area Silicates, *J. Am. Chem. Soc.* 137 (2015) 8096–8112. doi:10.1021/jacs.5b00622.
- [16] A. Kumar, B.J. Walder, A. Kunhi Mohamed, A. Hofstetter, B. Srinivasan, A.J. Rossini, K. Scrivener, L. Emsley, P. Bowen, The Atomic-Level Structure of Cementitious Calcium Silicate Hydrate, *J. Phys. Chem. C*. 121 (2017) 17188–17196. doi:10.1021/acs.jpcc.7b02439.
- [17] T. Gutmann, A. Grünberg, N. Rothermel, M. Werner, M. Srou, S. Abdhussain, S. Tan, Y. Xu, H. Breitzke, G. Buntkowsky, Solid-state NMR concepts for the investigation of supported transition metal catalysts and nanoparticles, *Solid State Nucl. Magn. Reson.* 55–56 (2013) 1–11. doi:10.1016/j.ssnmr.2013.06.004.
- [18] C. Copéret, W.-C. Liao, C.P. Gordon, T.-C. Ong, Active Sites in Supported Single-Site Catalysts: An NMR Perspective, *J. Am. Chem. Soc.* 139 (2017) 10588–10596. doi:10.1021/jacs.6b12981.
- [19] T. Kobayashi, D. Singappuli-Arachchige, Z. Wang, I.I. Slowing, M. Pruski, Spatial distribution of organic functional groups supported on mesoporous silica nanoparticles: a study by conventional and DNP-enhanced ^{29}Si solid-state NMR, *Phys. Chem. Chem. Phys.* 19 (2017) 1781–1789. doi:10.1039/C6CP07642D.
- [20] M. Valla, A.J. Rossini, M. Caillot, C. Chizallet, P. Raybaud, M. Digne, A. Chaumonnot, A. Lesage, L. Emsley, J.A. van Bokhoven, C. Copéret, Atomic Description of the Interface between Silica and Alumina in Aluminosilicates through Dynamic Nuclear Polarization Surface-Enhanced NMR Spectroscopy and First-Principles Calculations, *J. Am. Chem. Soc.* 137 (2015) 10710–10719. doi:10.1021/jacs.5b06134.
- [21] H. Eckert, Amorphous Materials, in: R.K. Harris, R.E. Wasylshen (Eds.), *Encycl. Magn. Reson.*, John Wiley & Sons, Ltd, 2007. doi:10.1002/9780470034590.emrstm0009.
- [22] M. Edén, Chapter Four - ^{27}Al NMR Studies of Aluminosilicate Glasses, in: G.A. Webb (Ed.), *Annu. Rep. NMR Spectrosc.*, Academic Press, 2015: pp. 237–331. doi:10.1016/bs.arnmr.2015.04.004.

- [23] M. Edén, NMR studies of oxide-based glasses, *Annu. Rep. Sect. C Phys. Chem.* 108 (2012) 177–221. doi:10.1039/C2PC90006H.
- [24] W.J. Malfait, W.E. Halter, R. Verel, ^{29}Si NMR spectroscopy of silica glass: T_1 relaxation and constraints on the Si–O–Si bond angle distribution, *Chem. Geol.* 256 (2008) 269–277. doi:10.1016/j.chemgeo.2008.06.048.
- [25] S. Björgvinsdóttir, B.J. Walder, N. Matthey, L. Emsley, Maximizing nuclear hyperpolarization in pulse cooling under MAS, *J. Magn. Reson.* (2019). doi:10.1016/j.jmr.2019.01.011.
- [26] S. Meiboom, D. Gill, Modified Spin-Echo Method for Measuring Nuclear Relaxation Times, *Rev. Sci. Instrum.* 29 (1958) 688–691. doi:10.1063/1.1716296.
- [27] F.H. Larsen, I. Farnan, ^{29}Si and ^{17}O QCPMG-MAS solid-state NMR experiments as an optimum approach for half-integer nuclei having long T_1 relaxation times, *Chem Phys Lett.* 357 (2002) 403–408. doi:DOI: 10.1016/S0009-2614(02)00520-1.
- [28] J.W. Wiench, V.S.-Y. Lin, M. Pruski, ^{29}Si NMR in solid state with CPMG acquisition under MAS, *J. Magn. Reson.* 193 (2008) 233–42. doi:10.1016/j.jmr.2008.05.007.
- [29] I. Hung, Z. Gan, On the practical aspects of recording wideline QCPMG NMR spectra, *J. Magn. Reson.* 204 (2010) 256–265. doi:10.1016/j.jmr.2010.03.001.
- [30] J.H. Baltisberger, B.J. Walder, E.G. Keeler, D.C. Kaseman, K.J. Sanders, P.J. Grandinetti, Communication: Phase incremented echo train acquisition in NMR spectroscopy, *J. Chem. Phys.* 136 (2012) 211104. doi:10.1063/1.4728105.
- [31] B.J. Walder, K.K. Dey, D.C. Kaseman, J.H. Baltisberger, P.J. Grandinetti, Sideband separation experiments in NMR with phase incremented echo train acquisition, *J. Chem. Phys.* 138 (2013) 174203. doi:10.1063/1.4803142.
- [32] D.J. Srivastava, J.H. Baltisberger, P. Florian, F. Fayon, R.A. Shakhovoy, M. Deschamps, N. Sadiki, P.J. Grandinetti, Correlating structural distributions in silica glass with two-dimensional J -resolved spectroscopy, *Phys. Rev. B.* 98 (2018) 134202. doi:10.1103/PhysRevB.98.134202.
- [33] W.J. Malfait, W.E. Halter, Increased ^{29}Si NMR sensitivity in glasses with a Carr–Purcell–Meiboom–Gill echotrain, *J. Non-Cryst. Solids.* 354 (2008) 4107–4114. doi:10.1016/j.jnoncrysol.2008.05.030.
- [34] E. Lippmaa, M. Maegi, A. Samoson, G. Engelhardt, A.R. Grimmer, Structural studies of silicates by solid-state high-resolution silicon-29 NMR, *J. Am. Chem. Soc.* 102 (1980) 4889–4893. doi:10.1021/ja00535a008.
- [35] G.E. Maciel, D.W. Sindorf, Silicon-29 NMR study of the surface of silica gel by cross polarization and magic-angle spinning, *J. Am. Chem. Soc.* 102 (1980) 7606–7607. doi:10.1021/ja00545a056.
- [36] J. Trébosc, J.W. Wiench, S. Huh, V.S.-Y. Lin, M. Pruski, Studies of organically functionalized mesoporous silicas using heteronuclear solid-state correlation NMR spectroscopy under fast magic angle spinning, *J. Am. Chem. Soc.* 127 (2005) 7587–93. doi:10.1021/ja0509127.
- [37] S. Smet, P. Verlooy, F. Saïdi, F. Taulelle, J.A. Martens, C. Martineau-Corcós, Solid-state NMR tools for the structural characterization of POSSiSils: ^{29}Si sensitivity improvement with MC-CP and 2D ^{29}Si – ^{29}Si DQ-SQ at natural abundance, *Magn. Reson. Chem.* 0 (n.d.). doi:10.1002/mrc.4800.
- [38] H. Lock, R.A. Wind, G.E. Maciel, N. Zumbulyadis, ^{29}Si dynamic nuclear polarization of dehydrogenated amorphous silicon, *Solid State Commun.* 64 (1987) 41–44.
- [39] M. Lelli, D. Gajan, A. Lesage, M.A. Caporini, V. Vitzthum, P. Miéville, F. Héroguel, F. Rascón, A. Roussey, C. Thieuleux, M. Boualleg, L. Veyre, G. Bodenhausen, C. Copéret, L. Emsley, Fast Characterization of Functionalized Silica Materials by Silicon-29 Surface-Enhanced NMR Spectroscopy Using Dynamic Nuclear Polarization, *J Am Chem Soc.* 133 (2011) 2104–2107.
- [40] O. Lafon, M. Rosay, F. Aussenac, X. Lu, J. Trébosc, O. Cristini, C. Kinowski, N. Touati, H. Vezin, J.-P. Amoureux, Beyond the Silica Surface by Direct Silicon-29 Dynamic Nuclear Polarization, *Angew Chem Int Ed.* 50 (2011) 8367–8370.
- [41] S. Björgvinsdóttir, B.J. Walder, A.C. Pinon, L. Emsley, Bulk Nuclear Hyperpolarization of Inorganic Solids by Relay from the Surface, *J. Am. Chem. Soc.* 140 (2018) 7946–7951. doi:10.1021/jacs.8b03883.
- [42] A.J. Rossini, A. Zagdoun, M. Lelli, D. Gajan, F. Rascón, M. Rosay, W.E. Maas, C. Copéret, A. Lesage, L. Emsley, One-hundred-fold overall sensitivity enhancements for Silicon-29 NMR spectroscopy of surfaces by dynamic nuclear polarization with CPMG acquisition, *Chem. Sci.* 3 (2011) 108–115. doi:10.1039/C1SC00550B.
- [43] E.D. Becker, J.A. Feretti, T.C. Farrar, Driven Equilibrium Fourier Transform Spectroscopy. A New Method for Nuclear Magnetic Resonance Signal Enhancement, *J. Am. Chem. Soc.* 91 (1969) 7784–7785. doi:10.1021/ja50001a068.
- [44] C. Carlotti, F. Taulelle, E. Aubay, Signal-to-noise enhancement when $T_2 \neq T_1$ a new investigation of the pulse sequence deft, *J. Chim. Phys. Phys.-Chim. Biol.* 95 (1998) 208–215. doi:10.1051/jcp:1998123.

- [45] M.D. Mann, B.F. Chmelka, Measurement of Dilute ^{29}Si Species in Solution Using a Large Volume Coil and DEFT NMR, *Anal. Chem.* 72 (2000) 5131–5135. doi:10.1021/ac000357l.
- [46] L.-F. Kao, V.J. Hruby, Suppression or differentiation of solvent resonance by a combination of DEFT with a two-dimensional sequence, *J. Magn. Reson.* 1969. 70 (1986) 394–407. doi:10.1016/0022-2364(86)90128-9.
- [47] C.M.J.V. Uijen, J.H.D. Boef, Driven-equilibrium radiofrequency pulses in NMR imaging, *Magn. Reson. Med.* 1 (1984) 502–507. doi:10.1002/mrm.1910010409.
- [48] J.H. Maki, G.A. Johnson, G.P. Cofer, J.R. MacFall, SNR improvement in NMR microscopy using DEFT, *J. Magn. Reson.* 1969. 80 (1988) 482–492. doi:10.1016/0022-2364(88)90243-0.
- [49] J.S. Waugh, Sensitivity in Fourier transform NMR spectroscopy of slowly relaxing systems, *J. Mol. Spectrosc.* 35 (1970) 298–305. doi:10.1016/0022-2852(70)90205-5.
- [50] P. Waldstein, W.E. Wallace, Driven Equilibrium Methods for Enhancement of Nuclear Transients, *Rev. Sci. Instrum.* 42 (1971) 437–440. doi:10.1063/1.1685122.
- [51] J. William, E. Wallace, Theory and Optimization of the Pulsed NMR Driven Equilibrium Technique, *J. Chem. Phys.* 54 (1971) 1425–1427. doi:10.1063/1.1674996.
- [52] R.R. Shoup, E.D. Becker, T.C. Farrar, The driven equilibrium fourier transform NMR technique: An experimental study, *J. Magn. Reson.* 1969. 8 (1972) 298–310. doi:10.1016/0022-2364(72)90046-7.
- [53] M. Piotto, M. Bourdonneau, K. Elbayed, J.-M. Wieruszkeski, G. Lippens, New DEFT sequences for the acquisition of one-dimensional carbon NMR spectra of small unlabelled molecules, *Magn. Reson. Chem.* 44 (2006) 943–947. doi:10.1002/mrc.1884.
- [54] M.H. Levitt, R. Freeman, NMR population inversion using a composite pulse, *J. Magn. Reson.* 1969. 33 (1979) 473–476. doi:10.1016/0022-2364(79)90265-8.
- [55] M.H. Levitt, Composite Pulses, in: *eMagRes*, American Cancer Society, 2007. doi:10.1002/9780470034590.emrstm0086.
- [56] T.-L. Hwang, P.C.M. van Zijl, M. Garwood, Broadband Adiabatic Refocusing without Phase Distortion, *J. Magn. Reson.* 124 (1997) 250–254. doi:10.1006/jmre.1996.1049.
- [57] J.M. Bohlen, G. Bodenhausen, Experimental Aspects of Chirp NMR Spectroscopy, *J. Magn. Reson. A* 102 (1993) 293–301. doi:10.1006/jmra.1993.1107.
- [58] K. Riedel, C. Herbst, J. Leppert, O. Ohlenschläger, M. Görlach, R. Ramachandran, Tailoring broadband inversion pulses for MAS solid state NMR, *J. Biomol. NMR.* 35 (2006) 275–83. doi:10.1007/s10858-006-9044-7.
- [59] G. Kervern, G. Pintacuda, L. Emsley, Fast adiabatic pulses for solid-state NMR of paramagnetic systems, *Chem. Phys. Lett.* 435 (2007) 157–162. doi:10.1016/j.cplett.2006.12.056.
- [60] B. Heise, J. Leppert, R. Ramachandran, REDOR with adiabatic dephasing pulses, *J. Magn. Reson.* 146 (2000) 181–187. doi:10.1006/jmre.2000.2129.
- [61] M. Garwood, Y. Ke, Symmetric pulses to induce arbitrary flip angles with compensation for rf inhomogeneity and resonance offsets, *J. Magn. Reson.* 1969. 94 (1991) 511–525. doi:10.1016/0022-2364(91)90137-I.
- [62] M. Garwood, L. DelaBarre, The Return of the Frequency Sweep: Designing Adiabatic Pulses for Contemporary NMR, *J. Magn. Reson.* 153 (2001) 155–177. doi:10.1006/jmre.2001.2340.
- [63] J. Leppert, B. Heise, M. Görlach, R. Ramachandran, REDOR: an assessment of the efficacy of dipolar recoupling with adiabatic inversion pulses, *J. Biomol. NMR.* 23 (2002) 227–38.
- [64] H. Nagashima, A.S. Lilly Thankamony, J. Trébosc, L. Montagne, G. Kerven, J.-P. Amoureux, O. Lafon, Observation of proximities between spin-1/2 and quadrupolar nuclei in solids: Improved robustness to chemical shielding using adiabatic symmetry-based recoupling, *Solid State Nucl. Magn. Reson.* 94 (2018) 7–19. doi:10.1016/j.ssnmr.2018.07.001.
- [65] D.I. Hoult, R.E. Richards, The Signal-to-Noise Ratio of the Nuclear Magnetic Resonance Experiment, *J. Magn. Reson.* 85 (1976) 71–85.
- [66] R.R. Ernst, Application of Fourier Transform Spectroscopy to Magnetic Resonance, *Rev. Sci. Instrum.* 37 (1966) 93. doi:10.1063/1.1719961.
- [67] M. Bak, J.T. Rasmussen, N.C. Nielsen, SIMPSON: a general simulation program for solid-state NMR spectroscopy, *J. Magn. Reson.* 147 (2000) 296–330. doi:10.1006/jmre.2000.2179.
- [68] M. Bak, N.C. Nielsen, REPULSION, A Novel Approach to Efficient Powder Averaging in Solid-State NMR, *J. Magn. Reson.* 125 (1997) 132–139.
- [69] H.C. Marsmann, ^{29}Si NMR, in: J.C. Lindon (Ed.), *Encycl. Spectrosc. Spectrom.*, Elsevier, Oxford, 1999: pp. 2031–2042. doi:10.1006/rwsp.2000.0277.
- [70] G. Engelhardt, Silicon-29 NMR of Solid Silicates, in: *eMagRes*, American Cancer Society, 2007. doi:10.1002/9780470034590.emrstm0506.

- [71] M.R. Hansen, H.J. Jakobsen, J. Skibsted, ^{29}Si chemical shift anisotropies in calcium silicates from high-field ^{29}Si MAS NMR spectroscopy, *Inorg. Chem.* 42 (2003) 2368–77. doi:10.1021/ic020647f.
- [72] D. Sakellariou, T. Charpentier, Shift Anisotropy Tensors in Amorphous Natural-Abundance Solids: High-Resolution ^{29}Si Chemical Shift Anisotropy Distributions under Very Slow Sample Rotation, *Appl. Magn. Reson.* 32 (2007) 583–594. doi:10.1007/s00723-007-0039-7.
- [73] D.H. Brouwer, G.D. Enright, Probing Local Structure in Zeolite Frameworks: Ultrahigh-Field NMR Measurements and Accurate First-Principles Calculations of Zeolite ^{29}Si Magnetic Shielding Tensors, *J. Am. Chem. Soc.* 130 (2008) 3095–3105. doi:10.1021/ja077430a.
- [74] P. Rejmak, J.S. Dolado, M.J. Stott, A. Ayuela, ^{29}Si Chemical Shift Anisotropies in Hydrated Calcium Silicates: A Computational Study, *J. Phys. Chem. C.* 117 (2013) 8374–8380. doi:10.1021/jp308787z.
- [75] R. West, J.D. Cavalieri, J.J. Buffy, C. Fry, K.W. Zilm, J.C. Duchamp, M. Kira, T. Iwamoto, T. Müller, Y. Apeloig, A Solid-State NMR and Theoretical Study of the Chemical Bonding in Disilenes, *J. Am. Chem. Soc.* 119 (1997) 4972–4976. doi:10.1021/ja963921b.
- [76] J.J. Buffy, R. West, M. Bendikov, Y. Apeloig, Chemical Shielding Tensors for a Silicon–Carbon Double Bond, *J. Am. Chem. Soc.* 123 (2001) 978–979. doi:10.1021/ja003389z.
- [77] S. Odedra, S. Wimperis, Imaging of the B_1 distribution and background signal in a MAS NMR probehead using inhomogeneous B_0 and B_1 fields, *J. Magn. Reson.* 231 (2013) 95–99. doi:10.1016/j.jmr.2013.04.002.
- [78] R. Gupta, G. Hou, T. Polenova, A.J. Vega, RF inhomogeneity and how it controls CPMAS, *Solid State Nucl. Magn. Reson.* 72 (2015) 17–26. doi:10.1016/j.ssnmr.2015.09.005.
- [79] H. Nagashima, J. Trébosc, O. Lafon, F. Pourpoint, P. Paluch, M.J. Potrzebowski, J.-P. Amoureux, Imaging the spatial distribution of radiofrequency field, sample and temperature in MAS NMR rotor, *Solid State Nucl. Magn. Reson.* 87 (2017) 137–142. doi:10.1016/j.ssnmr.2017.08.001.
- [80] R. Tycko, Broadband Population Inversion, *Phys. Rev. Lett.* 51 (1983) 775. doi:10.1103/PhysRevLett.51.775.
- [81] R. Tycko, H.M. Cho, E. Schneider, A. Pines, Composite pulses without phase distortion, *J. Magn. Reson.* 1969. 61 (1985) 90–101. doi:10.1016/0022-2364(85)90270-7.
- [82] a J. Shaka, a Pines, Symmetric phase-alternating composite pulses, *J. Magn. Reson.* 1969. 71 (1987) 495–503. doi:10.1016/0022-2364(87)90249-6.
- [83] S. Wimperis, Iterative schemes for phase-distortionless composite 180° pulses, *J. Magn. Reson.* 1969. 93 (1991) 199–206. doi:10.1016/0022-2364(91)90043-S.
- [84] S. Odedra, S. Wimperis, Use of composite refocusing pulses to form spin echoes., *J. Magn. Reson.* 214 (2012) 68–75. doi:10.1016/j.jmr.2011.10.006.
- [85] S. Odedra, M.J. Thrippleton, S. Wimperis, Dual-compensated antisymmetric composite refocusing pulses for NMR, *J. Magn. Reson.* 225 (2012) 81–92. doi:10.1016/j.jmr.2012.10.003.
- [86] R. Freeman, S.P. Kempell, M.H. Levitt, Radiofrequency pulse sequences which compensate their own imperfections, *J. Magn. Reson.* 1969. 38 (1980) 453–479. doi:10.1016/0022-2364(80)90327-3.
- [87] S. Wegner, L. van Wüllen, G. Tricot, The structure of phosphate and borosilicate glasses and their structural evolution at high temperatures as studied with solid state NMR spectroscopy: Phase separation, crystallisation and dynamic species exchange, *Solid State Sci.* 12 (2010) 428–439. doi:10.1016/j.solidstatesciences.2009.03.021.
- [88] I.I. Slowing, B.G. Trewyn, S. Giri, V.S.-Y. Lin, Mesoporous Silica Nanoparticles for Drug Delivery and Biosensing Applications, *Adv. Funct. Mater.* 17 (2007) 1225–1236. doi:10.1002/adfm.200601191.
- [89] B. Gardelle, S. Duquesne, C. Vu, S. Bourbigot, Thermal degradation and fire performance of polysilazane-based coatings, *Thermochim. Acta.* 519 (2011) 28–37. doi:10.1016/j.tca.2011.02.025.
- [90] P. Florian, F. Fayon, D. Massiot, ^2Si –O–Si Scalar Spin–Spin Coupling in the Solid State: Crystalline and Glassy Wollastonite CaSiO_3 , *J. Phys. Chem. C.* 113 (2009) 2562–2572. doi:10.1021/jp8078309.
- [91] O. Lafon, A.S. Lilly Thankamony, T. Kobayashi, D. Carnevale, V. Vitzthum, I.I. Slowing, K. Kandel, H. Vezin, J.-P. Amoureux, G. Bodenhausen, M. Pruski, Mesoporous Silica Nanoparticles Loaded with Surfactant: Low Temperature Magic Angle Spinning ^{13}C and ^{29}Si NMR Enhanced by Dynamic Nuclear Polarization, *J Phys Chem C.* 117 (2013) 1375–1382. doi:10.1021/jp310109s.
- [92] T. Kobayashi, O. Lafon, A.S. Lilly Thankamony, I.I. Slowing, K. Kandel, D. Carnevale, V. Vitzthum, H. Vezin, J.-P. Amoureux, G. Bodenhausen, M. Pruski, Analysis of Sensitivity Enhancement by Dynamic Nuclear Polarization in Solid-State NMR: a Case Study of Functionalized Mesoporous Materials., *Phys. Chem. Chem. Phys.* PCCP. 15 (2013) 5553–5562. doi:10.1039/c3cp00039g.

Improved sensitivity and quantification for ^{29}Si NMR experiments on solids using UDEFT (Uniform Driven Equilibrium Fourier Transform)

Nghia Tuan Duong,^{1,#} Julien Trébosc,^{1,2*} Olivier Lafon,^{1,3} Jean-Paul Amoureux^{1,4*}

Supporting Information

¹ Univ. Lille, Centrale Lille, ENSCL, Univ. Artois, CNRS-8181, UCCS – Unit of Catalysis and Chemistry of Solids, F-59000 Lille, France.

² Univ. Lille, CNRS-FR2638, Fédération Chevreul, F-59000 Lille, France.

³ Institut Universitaire de France, 1 rue Descartes, F-75231 Paris, France.

⁴ Bruker Biospin, 34 rue de l'industrie, F-67166 Wissembourg, France.

Present address: RIKEN-JEOL Collaboration Center, Yokohama, Kanagawa 230-0045, Japan.

I. Derivation of Eqs. 3 and 9

For both UDEFT and SP sequences, the longitudinal magnetization after $n \leq NS$ scans at the beginning of the τ_{RD} delay is denoted M_n . It relaxes during τ_{RD} to the $M_{R,n}$ longitudinal magnetization given by:

$$M_{R,n} = M_n e^{-\Psi} + M_\infty (1 - e^{-\Psi}) \quad (\text{S1})$$

where Ψ is defined in Eq. 4.

I-1. UDEFT sequence

I-1-1. Magnetization

For UDEFT sequence, the longitudinal magnetization after $n+1$ scans is equal to:

$$M_{n+1} = E \cdot M_{R,n} \quad (\text{S2})$$

where the UDEFT efficiency E is given by Eq. 5. From Eqs.S1 and S2, we can deduce the following recurrence relation:

$$M_{n+1} = E \{ M_n e^{-\Psi} + M_\infty (1 - e^{-\Psi}) \} = B + C M_n \quad (\text{S4})$$

with

$$B = E \cdot M_\infty (1 - e^{-\Psi}) \text{ and } C = E e^{-\Psi} \quad (\text{S5})$$

Eq. S4 is a first-order linear difference equation and M_n can be expressed as

$$M_n = \frac{B}{1-C} + \left\{ M_0 - \frac{B}{1-C} \right\} C^n \quad (\text{S6})$$

I-1-2. Signal to noise ratio

The signal of the n^{th} scan, s_n , is proportional to the $M_{R,n}$ magnetization

$$s_n = D M_{R,n} \quad (\text{S7})$$

where D is a constant subsuming several factors, such as coil geometry, filling factor, Larmor frequency and apodization [1]. Using Eq. S2, the s_n signal can also be written

$$s_n = \frac{D}{E} M_n \quad (\text{S8})$$

The total signal after the NS scans, S_{NS} , of the UDEFT experiment can be expressed as

$$S_{NS} = \sum_{n=1}^{NS} s_n = \frac{D}{E} \sum_{n=1}^{NS} M_n \quad (S9)$$

using Eq. S8. By substituting Eq. S6 into Eq. S9, S_{NS} appears as the sum of an arithmetic series and a geometric one with a common ratio C and can thus be written as

$$S_{NS} = \frac{D}{E} \left\{ NS \frac{B}{1-C} + \left\{ M_0 - \frac{B}{1-C} \right\} \frac{1-C^{NS}}{1-C} \right\} \quad (S10)$$

By substituting B and C constants by their expressions given in Eq. S5, we obtain

$$S^{\text{UDEFT}}(NS) = D \left(e^{-\psi} \left\{ M_0 - \frac{EM_{\infty}(1-e^{-\psi})}{1-Ee^{-\psi}} \right\} \frac{1-(Ee^{-\psi})^{NS}}{1-Ee^{-\psi}} + NS \frac{M_{\infty}(1-e^{-\psi})}{1-Ee^{-\psi}} \right) \quad (S11)$$

This equation is the sum of two contributions. The last term corresponds to the steady-state regime and provides the same signal every scan. The first term corresponds to transient signals and rapidly converges to a constant value when $NS \gg 1$, $(Ee^{-\psi})^{NS} \rightarrow 0$, and thus the accumulated signal becomes:

$$S^{\text{UDEFT}}(NS \gg 1) = D \left(e^{-\psi} \frac{M_0 - EM_{\infty} + Ee^{-\psi}(M_{\infty} - M_0)}{(1-Ee^{-\psi})^2} + NS \frac{M_{\infty}(1-e^{-\psi})}{1-Ee^{-\psi}} \right) \quad (S12)$$

Assuming the noise in UDEFT experiment is mainly random, its root-mean-square (rms) amplitude is proportional to \sqrt{NS} :

$$N(NS) = N(1)\sqrt{NS} \quad (S13)$$

where $N(1)$ is the rms amplitude of the noise for a single scan. This amplitude depends on the temperature of the coil, its resistance and the bandwidth of the receiver [1]. The S/N can be calculated by dividing Eq. S11 by Eq. S13, which yields Eq. 6 with $K = D/N(1)$.

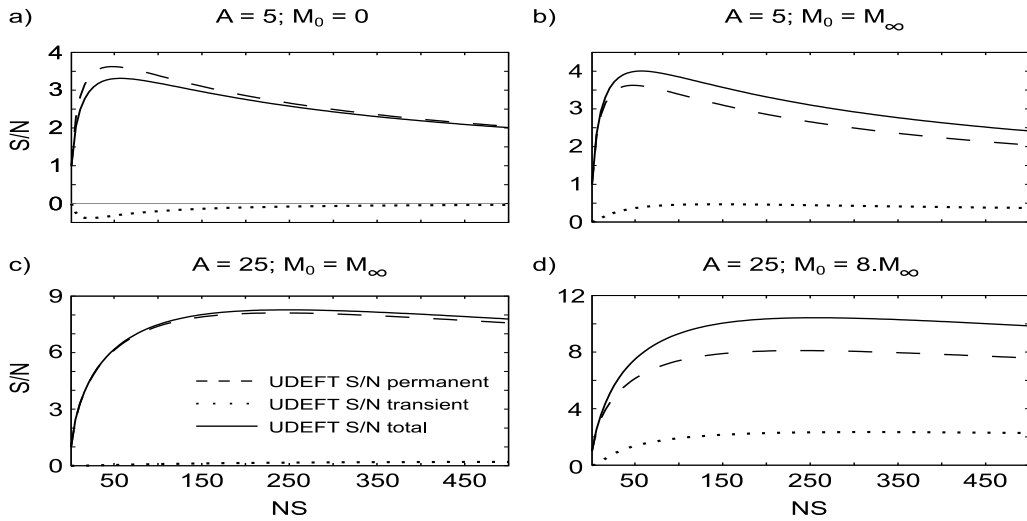


Fig.S1. Plot of total S/N ratio (continuous line) of UDEFT experiment as well as the contributions to S/N of transient regime (dotted line) and steady-state one (dashed line) as function of NS for $E = 90\%$ and $A = (a,b) 5$ or $(c,d) 25$. The initial magnetization is $M_0 = 0$ (a), M_{∞} , (b,c) or $8M_{\infty}$. (d). The total S/N ratio, the transient contribution and the steady-state one were calculated using Eq. 6, the first term and the second one, respectively, with $K = M_{\infty} = 1$.

I-2. SP sequence

I-2-1. Magnetization

After the n^{th} θ pulse of SP experiments, the longitudinal magnetization is given by

$$M_{n+1} = \cos(\theta)M_{R,n} \quad (S14)$$

By combining Eqs. S1 and S14, we obtain

$$M_{n+1} = \cos(\theta) \{ M_n e^{-\Psi} + M_{\infty}(1 - e^{-\Psi}) \} = B' + C'M_n \quad (S15)$$

with

$$B' = \cos(\theta)M_\infty(1 - e^{-\Psi}) \text{ and } C' = \cos(\theta)e^{-\Psi} \quad (\text{S16})$$

Eq. S15 is similar to Eq. S4 and hence, M_n can be expressed as

$$M_n = \frac{B'}{1-C'} + \left\{ M_0 - \frac{B'}{1-C'} \right\} C'^n. \quad (\text{S17})$$

I-2-2. Signal to noise ratio

The signal of the n^{th} scan, s_n , is given by

$$s_n = D \sin(\theta) M_{R,n} \quad (\text{S18})$$

By substituting Eq. S1 into Eq. S18, we find that the total signal $S_{NS} = \sum_{n=1}^{NS} s_n$ is equal to

$$S_{NS} = D \sin(\theta) \left[e^{-\Psi} \left\{ M_0 - \frac{\cos(\theta)M_\infty(1-e^{-\Psi})}{1-\cos(\theta)e^{-\Psi}} \right\} \frac{1-(\cos(\theta)e^{-\Psi})^{NS}}{1-\cos(\theta)e^{-\Psi}} + NS \frac{M_\infty(1-e^{-\Psi})}{1-\cos(\theta)e^{-\Psi}} \right] \quad (\text{S19})$$

Eq. S13 is still valid for SP experiment and the S/N ratio is given by Eq. 7.

I-3. Quantitative measurements

For UDEFT, by substituting Eqs. S1 and S2 into Eq. 9, we obtain

$$m = m.E.e^{-\Psi} + (1 - e^{-\Psi}) \quad (\text{S20})$$

which can be recast into Eq. 10. For SP, an equation similar to Eq. S20 with E replaced by $\cos(\theta)$ can be obtained by substituting Eqs. S1 and S14 into Eq. 6 and can be recast into Eq. 11.

II. Numerical simulations

II-1. Optimization of composite π -pulses

II-1-1. Robustness to rf-field and offset for the refocusing π -pulse

Refocusing π -pulse	Ref.	$\theta_{\text{tot}} / ^\circ$	Rotation	Compensation	$\frac{\Delta v_1}{v_{1\text{nom}}} \text{ (a)}$	$\frac{\Delta v_0}{v_{1\text{nom}}} \text{ (b)}$
180 ₀ (P180 _x)		180	variable		0.86	0.46
59 ₁₈₀ 298 ₀ 59 ₁₈₀ (CP _{x1})	[2]	416	constant	v_0	0.86	0.86
58 ₀ 140 ₁₈₀ 344 ₀ 140 ₁₈₀ 58 ₀ (CP _{x2})	[2]	740	constant	v_0	0.86	1.11
180 ₁₂₀ 180 ₂₄₀ 180 ₁₂₀ (CP _{x3})	[3]	540	constant	v_1	<i>0.76</i>	<i>0.31</i>
90 ₉₀ 180 ₀ 90 ₉₀ (CP _{x4})	[4]	360	variable	v_1	<i>0.29</i>	0.51
90 ₀ 360 ₁₂₀ 90 ₀ (CP _{x5})	[5]	540	variable	v_1	<i>0.14</i>	0.80
180 _{104.5} 360 _{313.4} 180 _{104.5} 180 ₀ (CP _{x6})	[6]	900	variable	v_1	0.86	0.60
90 ₀ 255 ₁₈₀ 315 ₀ (CP _{x7})	[7]	660	variable	v_0	0.86	<i>0.23</i>

Table S1. Robustness to rf-field and offset of UDEFT using the refocusing pulses listed in the first column. The ranges of rf-fields and offsets yielding $E_{\text{rf}} \geq 90\%$ were determined using spin-dynamics simulations with $v_R = 4$ kHz and $v_{1\text{nom}} = 70$ kHz. In these simulations, all pulses of UDEFT are ideal, except for the refocusing π -pulse. Bandwidths which are extended with respect to 180₀ are in bold type, whereas those which are smaller are in italics. ^(a) Range of rf-fields for which $E_{\text{rf}} \geq 90\%$, normalized with respect to $v_{1\text{nom}}$. The v_1 values yielding $E_{\text{rf}} = 90\%$ are symmetrical with respect to $v_{1\text{nom}}$. ^(b) Range of

offsets for which $E_{rf} \geq 90\%$ normalized with respect to resonance frequency. The offset values yielding $E_{rf} = 90\%$ are symmetrical with respect to resonance frequency, except for CP_{x6} , for which a slight asymmetry is observed.

II-1-2. Robustness to rf-field and offset for the inversion π -pulses

Inversion π -pulse	Ref.	$\theta_{tot} / ^\circ$	Rotation	Compensation	$\frac{\Delta v_1}{v_{1nom}}$ (a)	$\frac{\Delta v_0}{v_{1nom}}$ (b)
180 ₀ (P180 _z)		180	variable		0.29	0.46
90 ₀ 240 ₉₀ 90 ₀ (CP _{z1})	[8]	420	variable	v_0 and v_1	0.61	1.29
90 ₉₀ 180 ₀ 90 ₉₀ (CP _{z2})	[4]	360	variable	v_1	0.63	0.51
180 ₁₂₀ 180 ₂₄₀ 180 ₁₂₀ (CP _{z3})	[3]	540	variable	v_1	0.83	0.23
58 ₀ 140 ₁₈₀ 344 ₀ 140 ₁₈₀ 58 ₀ (CP _{z4})	[2]	740	constant	v_0	0.29	1.00
59 ₁₈₀ 298 ₀ 59 ₁₈₀ (CP _{z5})	[2]	416	constant	v_0	0.29	0.74
90 ₀ 360 ₁₂₀ 90 ₀ (CP _{z6})	[5]	540	variable	v_1	0.83	0.40

Table S2. Robustness to rf-field and offset of UDEFT using the inversion pulses listed in the first column. The ranges of rf-fields and offsets yielding $E_{rf} \geq 90\%$ were determined using spin dynamics simulations with $v_R = 4$ kHz and $v_{1nom} = 70$ kHz. In these simulations, all pulses are ideal, except for the inversion π -pulse. Bandwidths which are extended with respect to 180₀ are in bold type, whereas those which are smaller are in italics. (a) Range of rf-fields for which $E_{rf} \geq 90\%$, normalized with respect to v_{1nom} . The v_1 values yielding $E_{rf} = 90\%$ are symmetrical with respect to v_{1nom} , except for CP_{z1} , for which an asymmetry is observed. (b) Range of offset values for which $E_{rf} \geq 90\%$ normalized with respect to resonance frequency.

II-1-3. Robustness to rf-field and offset for the pairs of composite π -pulses

Combination of pulses	$E_{rf} \geq 90\%$		$E_{rf} \geq 98\%$	
	$\frac{\Delta v_1}{v_{1nom}}$ (a)	$\frac{\Delta v_0}{v_{1nom}}$ (b)	$\frac{\Delta v_1}{v_{1nom}}$ (a)	$\frac{\Delta v_0}{v_{1nom}}$ (b)
P180 _x -P180 _z	0.29	0.77	0.14	0.49
P180 _x -CP _{z1}	0.61	0.40	0.44	0.16
P180 _x -CP _{z2}	0.63	0.80	0.43	0.50
CP _{x1} -P180 _z	0.29	0.57	0.14	0.21
CP _{x1} -CP _{z1}	0.61	0.93	0.44	0.56
CP _{x1} -CP _{z2}	0.63	0.83	0.43	0.21
CP _{x2} -P180 _z	0.29	0.47	0.14	0.24
CP _{x2} -CP _{z1}	0.61	1.20	0.44	1.10
CP _{x2} -CP _{z2}	0.63	0.51	0.43	0.23

Table S3. Robustness to rf-field and offset of UDEFT using the combination of refocusing and inversion pulses listed in the first column. The ranges of rf-fields and offsets yielding $E_{rf} \geq 90\%$ or 98% were determined using spin dynamics simulations with $v_R = 4$ kHz and $v_{1nom} = 70$ kHz. In these simulations, all pulses have a finite length. Bandwidths which are extended with

respect to 180° are in bold type. Bandwidths which are contracted with respect to 180° are in italics. (a) Range of rf fields for which $E_{rf} \geq 90\%$ (2nd column) and 98% (4th column) normalized with respect to v_{1nom} . The v_1 values yielding $E_{rf} = 90$ and 98 % are symmetrical with respect to v_{1nom} . (b) Range of offsets for which $E_{rf} \geq 90\%$ (3rd column) and 98% (5th column) normalized with respect to resonance frequency.

II-1-4. Robustness to CSA for the composite π -pulses

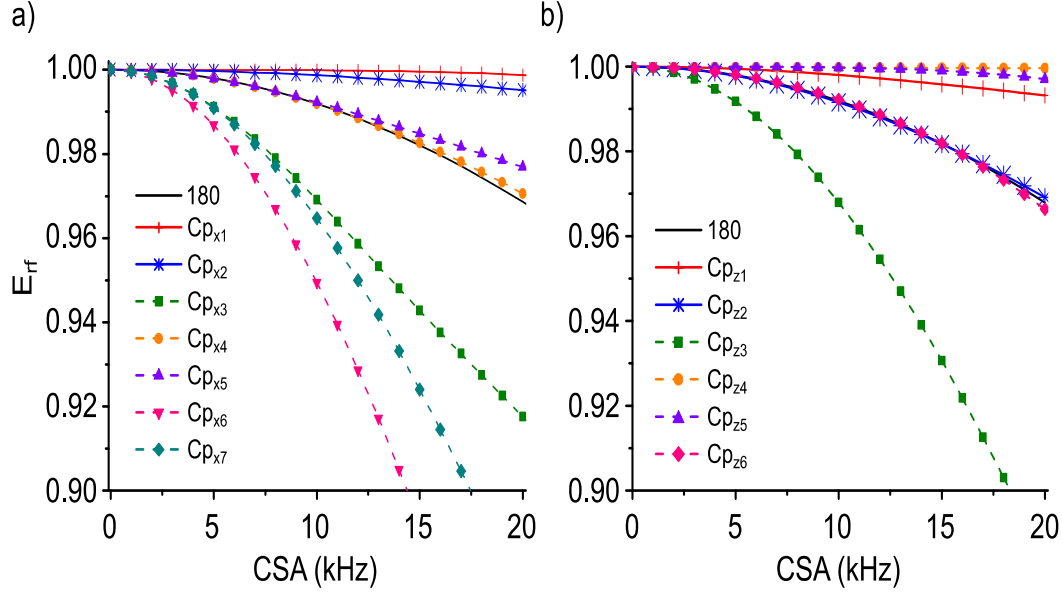


Fig.S2. Robustness to CSA of UDEFT using the (a) refocusing and (b) inversion composite π -pulses listed in Tables S1 and S2. All pulses were applied on resonance using $v_{1nom} = 70$ kHz with $v_R = 4$ kHz. In these simulations, all pulses were ideal, except the (a) refocusing or (b) inversion composite π -pulses.

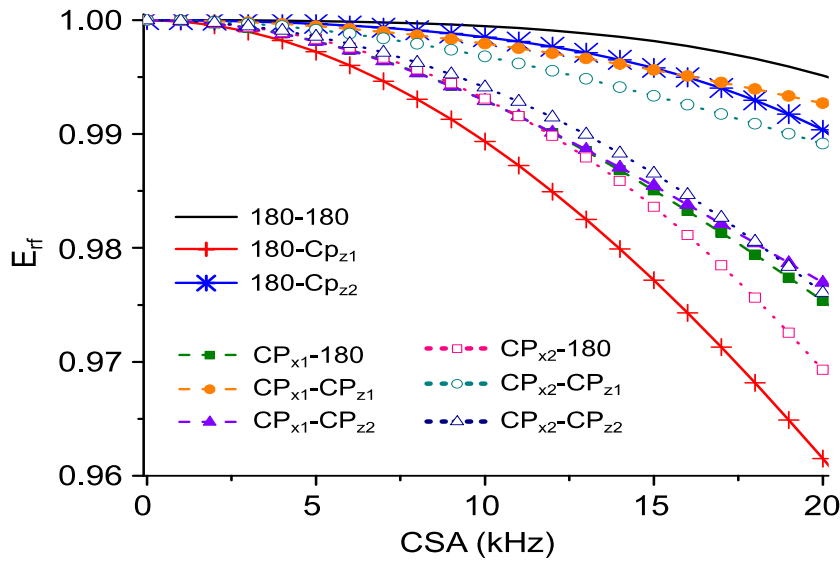


Fig.S3. Robustness to CSA of UDEFT using different pairs of refocusing-inversion composite π -pulses listed in Table S3. All pulses were applied on resonance using $v_{1nom} = 70$ kHz with $v_R = 4$ kHz. In these simulations, all pulses have a finite length.

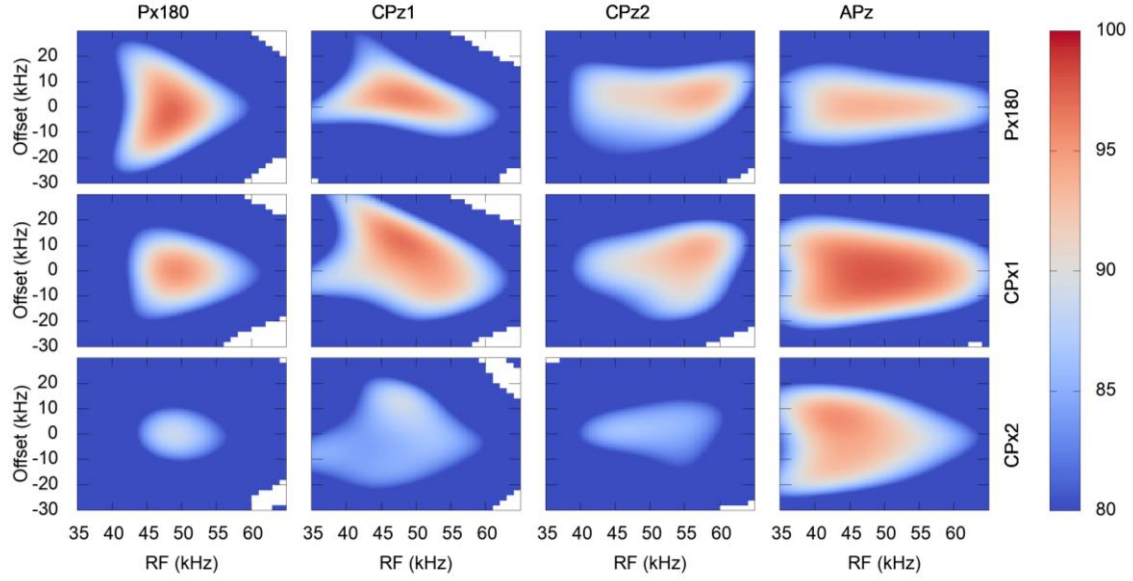


Fig.S4. Simulated E_{rf} efficiency versus rf-field and offset for UDEFT schemes using the refocusing and inversion pulses indicated on the right and the top of the figure, respectively. Simulations were performed for ^{29}Si CSA of 20 kHz, i.e. 250 ppm at $B_0 = 9.4$ T with $\nu_{\text{1nom}} = 50$ kHz and $\nu_R = 10$ kHz. In these simulations, all pulses have a finite length. The plotted E_{rf} efficiency corresponds to the geometric average of E_{rf} efficiencies of two successive scans, for which the phases of both refocusing and inversion pulses are incremented by 180° (see caption of Fig.4).

II-2. Stimulated echoes and phase cycling

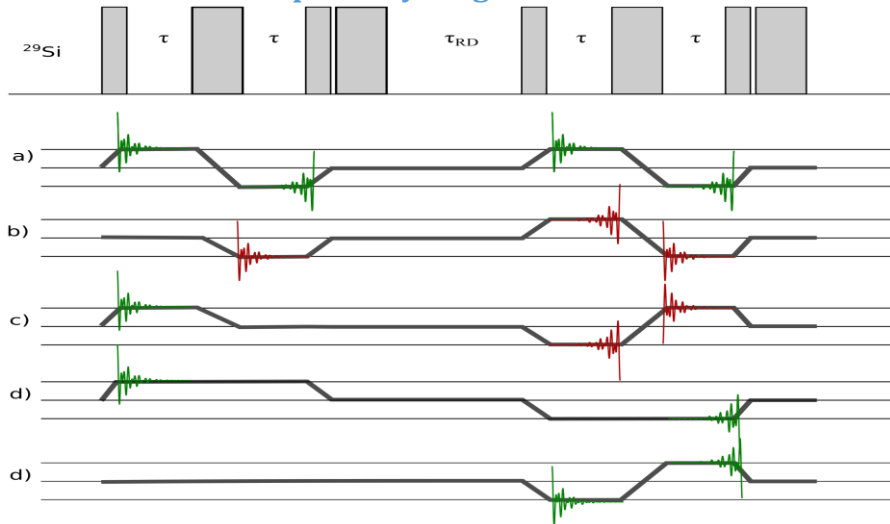


Fig.S5. (a-e) Examples of coherence transfer pathways leading to observable signals during the τ delays. The pulses and delays corresponding to two successive scans of UDEFT are displayed on the top. The FIDs contributing to the wanted signals are displayed in green, whereas those producing artifacts are displayed in red. (a) One of the desired coherence transfer pathways. (b-c) Coherence transfer pathways producing artifacts. (b) The contribution of the 1st FID to the detected signal is eliminated by the two-step phase cycling described in the caption of Fig.1. However, the 2nd and 3rd FIDs in (b) and (c) correspond to $\Delta p = \pm 2$ for the refocusing pulse as for the desired coherence transfer pathway and hence, cannot be removed by the phase cycle. (d,e) Coherence transfer pathways resulting from pulse imperfections, which do not produce artifacts in the UDEFT spectrum. Symmetric coherence transfer pathways produce identical signals.

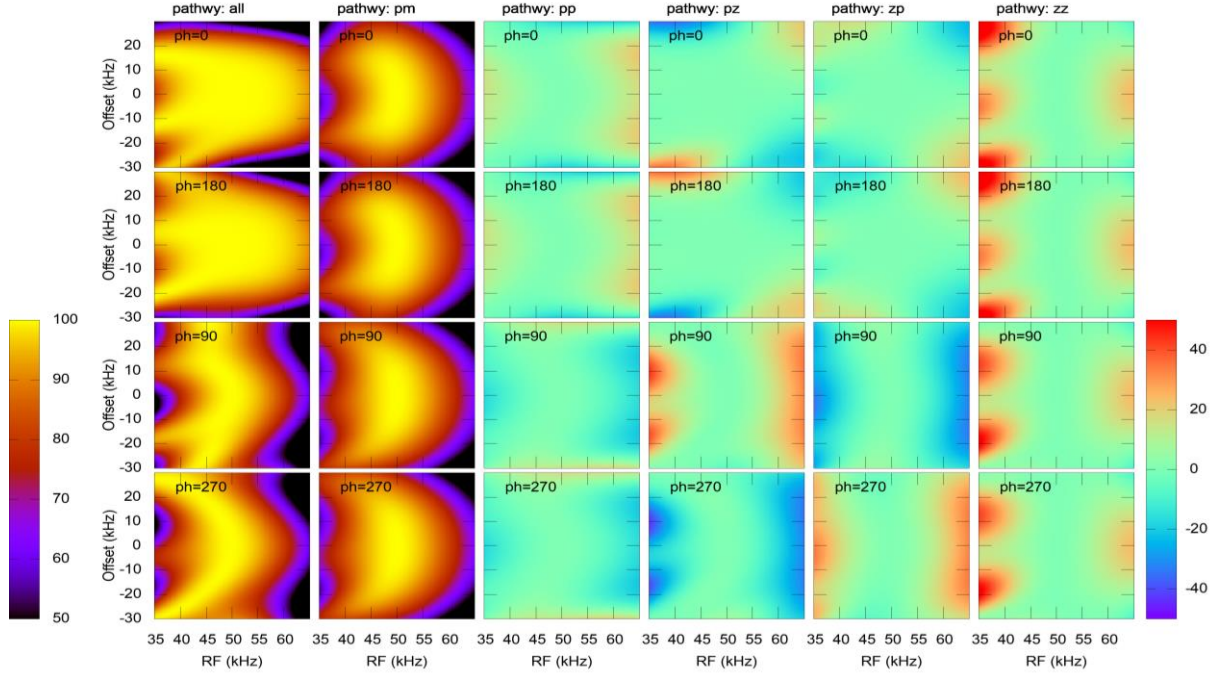


Fig.S6. Simulated E_{eff} efficiency versus rf-field and offset for UDEFT using CP_{x1} as refocusing pulse and AP_z as inversion pulse without a selection of coherence transfer pathway (1st column), with coherence orders during the 1st and 2nd τ delays equal to +1 and -1 (2nd column), +1 and +1 (3rd column), +1 and 0 (4th column), 0 and +1 (5th column), and 0 and 0 (6th column). The phases of the refocusing pulse is 0, 180°, 90°, 270° for rows 1, 2, 3, 4 respectively. The second $\pi/2$ -pulse phase was reversed when the refocusing pulse phase was 90° or 270°. The UDEFT sequences are: $90_{90}-\tau_0-(\text{CP}_{x1})_0-\tau_0-90_{90}-\text{AP}_z$, $90_{90}-\tau_0-(\text{CP}_{x1})_{180}-\tau_0-90_{90}-\text{AP}_z$, $90_{90}-\tau_{180}-(\text{CP}_{x1})_{90}-\tau_{180}-90_{270}-\text{AP}_z$, and $90_{90}-\tau_{180}-(\text{CP}_{x1})_{270}-\tau_{180}-90_{270}-\text{AP}_z$, for the 1st, 2nd, 3rd, and 4th row, respectively, where the subscript after τ denotes the phase of the receiver. $B_0 = 9.4$ T, $\nu_{1\text{nom}} = 50$ kHz, $\nu_R = 10$ kHz, $\text{CSA} = 0$.

VI III. Experimental results

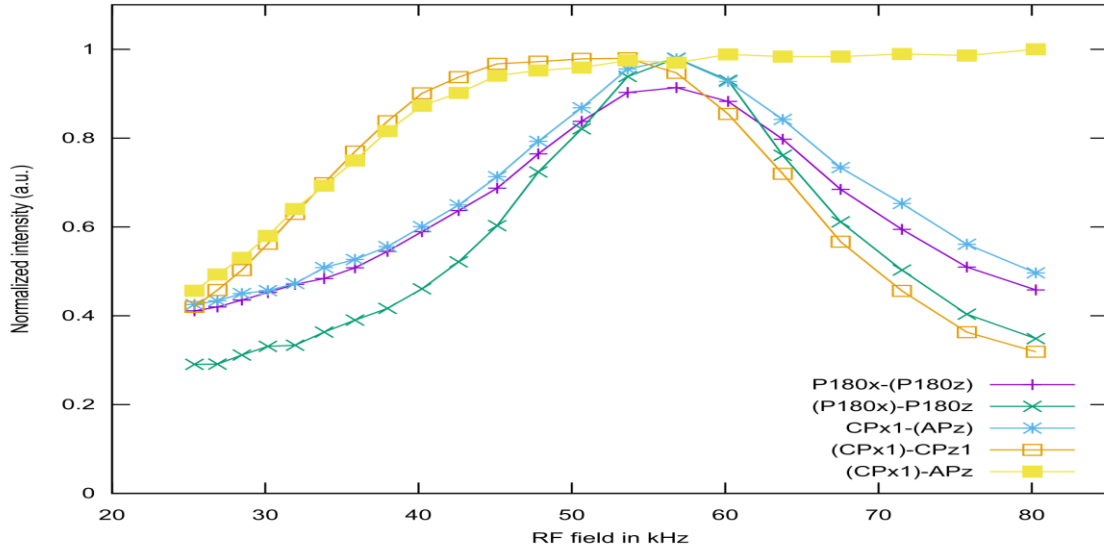


Fig.S7. Experimental ^{29}Si UDEFT signal of ^{29}Si -enriched amorphous silica sample versus the rf-amplitude of the refocusing and inversion π -pulses. For each such pair one rf-field (that with parentheses) was fixed at $\nu_1 = 57$ kHz (62.5 kHz for AP_z), whereas the other was changed about this nominal value. $\nu_1 = 57$ kHz was also used for the $\pi/2$ -pulses. For AP_z , $\tau_p = 50$ μs and $\Delta\nu_{0,\text{max}} = 4$ MHz. $B_0 = 9.4$ T, $\nu_R = 10$ kHz, $\tau = 2$ ms, $\text{NS} = 16$, $\tau_{\text{RD}} = 1$ s.

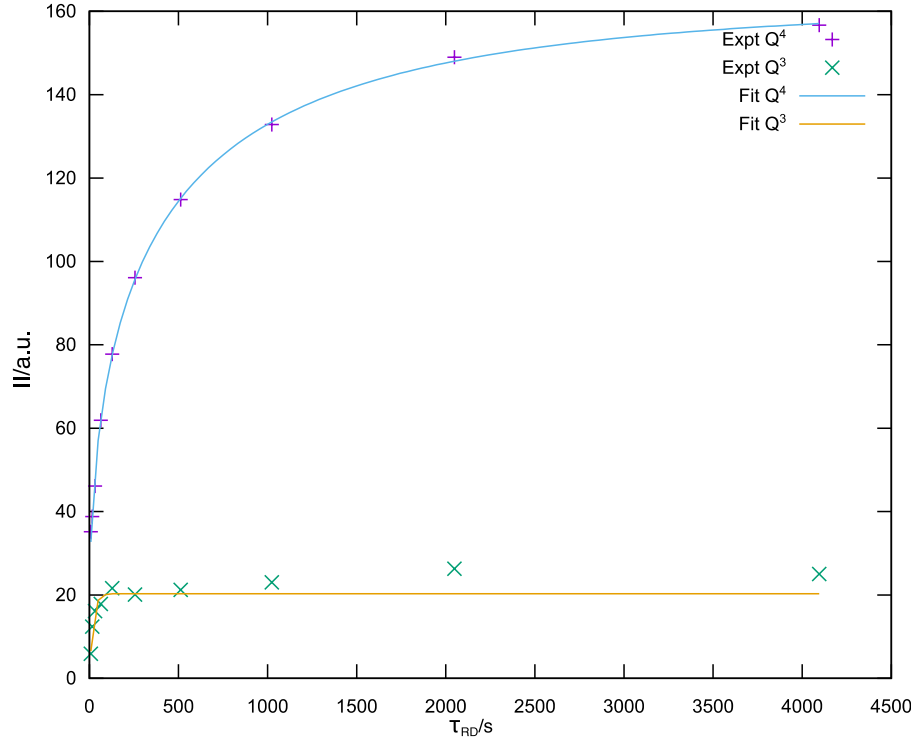


Fig.S8. Experimental build-up curves of ^{29}Si saturation-recovery Q^3 and Q^4 integrated intensities of SBA-15. The continuous lines are the best-fits of the experimental intensities to a stretched exponential function, $I(\tau) = I_{\infty}\{1 - \exp[-(\tau_{\text{RD}}/T_1)^{\beta}]\}$, where I_{∞} is the asymptotic integrated intensity for $\tau \gg T_1$ and $\beta \leq 1$. The best-fit parameters $\{I_{\infty}, \beta, T_1\}$ for Q^3 and Q^4 signals are $\{20, 1, 19 \text{ s}\}$ and $\{162, 0.52, 394 \text{ s}\}$, respectively. Q^3 and Q^4 sites were deconvoluted using DMFIT. After saturation and recovery, 128 transients were recorded using UDEFT sequence with a 1s repetition rate.

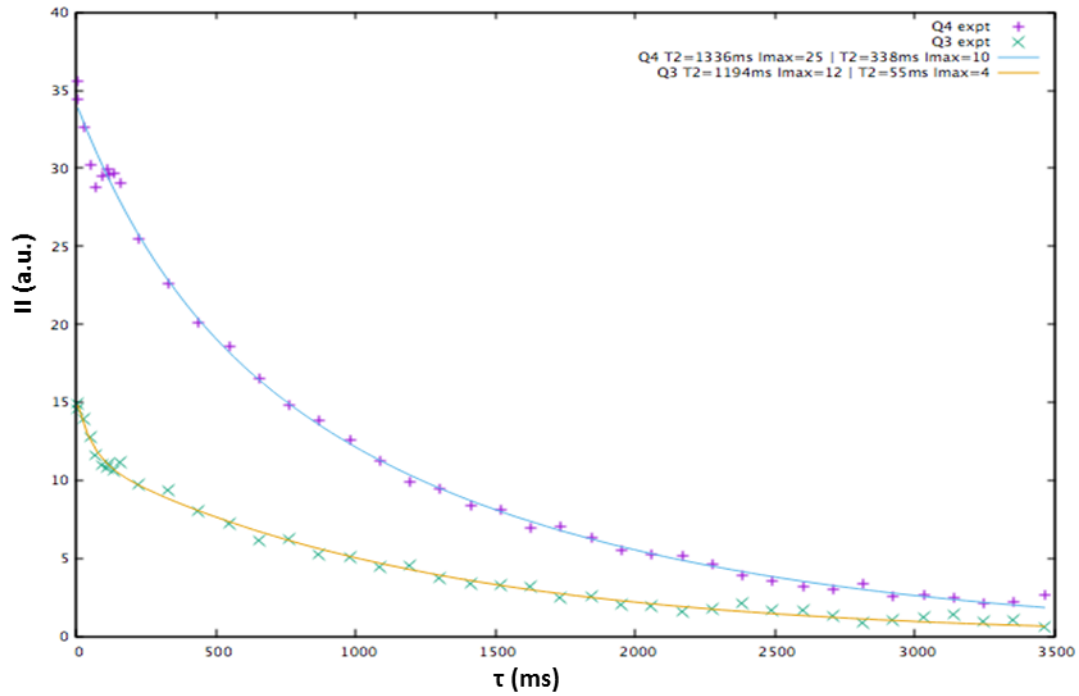


Fig.S9. Experimental decay of ^{29}Si spin-echo Q^3 and Q^4 integrated intensities (using DMFIT) of SBA-15 versus the echo delay, τ . After the echo sequence, magnetization was detected during a CPMG acquisition. The continuous lines are the best-fits of the experimental intensities to a bi-exponential function $I(\tau) = I_{s,\infty} \cdot \exp(-\tau/T'_{2s}) + I_{f,\infty} \cdot \exp(-\tau/T'_{2f})$ where $I_{i,\infty}$ with $i = s$ or f is the asymptotic integrated intensity for $\tau \gg T_{2i}'$ corresponding to the slow and fast components, respectively. The best-fit parameters $\{I_{f,\infty}, T_{2f}', I_{s,\infty}, T_{2s}'\}$ for Q^3 and Q^4 signals are $\{4, 0.05 \text{ s}, 12, 1.19 \text{ s}\}$ and $\{10, 0.34 \text{ s}, 25, 1.34 \text{ s}\}$, respectively.

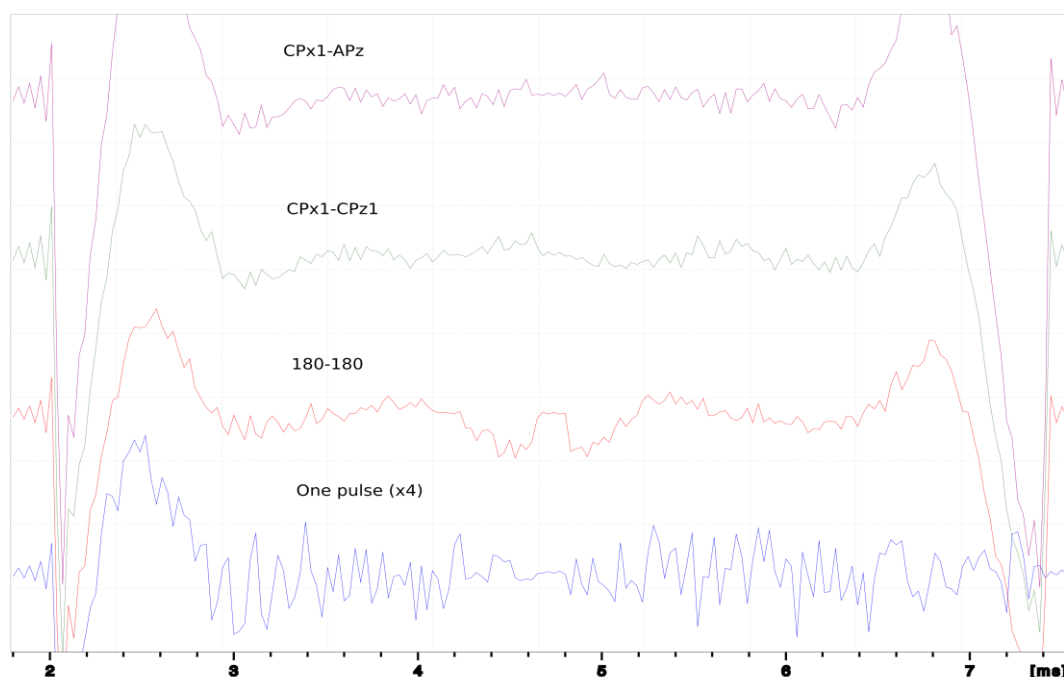


Fig.S10. Experimental FIDs of SBA-15 during the two τ delays of UDEFT using $CP_{x1}-AP_z$, $CP_{x1}-CP_{z1}$ and $P180_x-P180_z$. The FID of SP experiment is also displayed during 2τ at the bottom. Experimental parameters are those of Fig.7.

EXP	D_1 (s)	D (%)	T^2 (%)	T^3 (%)	S/N (D)	S/N (T^3)
ZG	180	7,9	15,3	76,8	33	96
UDEFT	12,5	9,5	15,9	74,6	28	62
"	25	8,5	15,8	75,7	32	82
"	50	8,0	15,0	77,1	38	106
"	75	7,4	15,2	77,4	36	106
"	100	7,1	15,3	77,7	42	130
"	150	6,9	15,6	77,4	38	119

Table.S4. Quantitative analysis of the proportions and S/Ns of the ^{29}Si MAS spectra of flame retardant material shown in Fig.9.

IV. Pulse sequences

The pulse sequences for various Bruker consoles are provided in a separate archive.

V. Simpson input files used for Figs. 4 and S4

The following Simpson input files were used for the Figs.4 and S4. A geometric average must be performed separately to account for the 2 phase cycling.

```
spinsys {
  channels  29Si
  nuclei    29Si
  shift     1 10000 10000 0 0 0 0
}
par {
  proton_frequency 400e6
}
```

```

spin_rate      10000
np             1
sw            10000
crystal_file   zcw88
gamma_angles   7
start_operator I1z
detect_operator I1z
variable rf0    50000
variable rflist 50000
variable isolist 10000
variable OneDone 1
# Adiabatic pulse RF factor:
# Adiabatic RF is ArfF * RF of nutation pulses
variable ArfF   1.0
verbose         0000
# num_cores     1
}

proc APz {rf phase {preparePhi 0} } {
    global par

    set Tinc 100e-3
    set Tp   50
    set n    [expr $Tp/$Tinc]

    if $preparePhi {
        set philist ""
        set rflist ""

        # other fixed shape pulse parameters
        set rf0AP [expr $par(rf0)*$par(ArfF)]
        set psi   10.0
        set K     atan(30)
        set Q     5

        set pi    [expr atan(1)*4]
        # wmax : max frequency offset from rf0AP and Q factor
        set wmax [expr tan($K)*$pi*$rf0AP**2*$Tp*(1e-6)/($K*$Q)]

        if $par(OneDone) {
            # wmax is printed once only
            puts "Offsetmax=$wmax"
            set par(OneDone) 0
        }

        for {set i 0} {$i<$n} {incr i 1} {
            set x [expr ($i+0.5)/$n]

            if {$i<$n/2} {
                set rfi [expr tanh(2*$psi*$x)]
            } else {
                set rfi [expr tanh(2*$psi*(1-$x))]
            }
            set phi [expr 360*$wmax*$Tp*(1e-6)*log(abs(cos($K*(1-2*$x))))/(2*tan($K)*$K)+$phase]

            set philist "$philist $phi"
            set rflist "$rflist $rfi"
        }
        return [list $rflist $philist]
    } #endif

    set rflist [lindex $par(ilist) 0]
    set philist [lindex $par(ilist) 1]

    for {set i 0} {$i<$n} {incr i 1} {
        pulse $Tinc [expr $rf*$par(ArfF)*[lindex $rflist $i]] [lindex $philist $i]
    }

    # test OK when printing derivative of phi with time one gets a tanhtan shape with max
    offset +-wmax
}

proc Px180 {rf phase {len 0}} {
    global par
    set p180 [expr 1e6/360*180/$par(rf0)]
    if { $len == "length" } {return [expr $p180]}
    pulse $p180 $rf [expr 0+$phase]
}

```

```

}

proc CPx1 {rf phase {len 0}} {
  global par
  set p59 [expr 1e6/360*59/$par(rf0)]
  set p298 [expr 1e6/360*298/$par(rf0)]

  if { $len == "length" } {return [expr 2*$p59+$p298]}

  pulse $p59 $rf [expr 180+$phase]
  pulse $p298 $rf [expr 0+$phase]
  pulse $p59 $rf [expr 180+$phase]
}

proc CPx2 {rf phase {len 0}} {
  global par
  set p58 [expr 1e6/360*58/$par(rf0)]
  set p140 [expr 1e6/360*140/$par(rf0)]
  set p344 [expr 1e6/360*344/$par(rf0)]

  if { $len == "length" } {return [expr 2*($p58+$p140)+$p344]}

  pulse $p58 $rf [expr 0+$phase]
  pulse $p140 $rf [expr 180+$phase]
  pulse $p344 $rf [expr 0+$phase]
  pulse $p140 $rf [expr 180+$phase]
  pulse $p58 $rf [expr 0+$phase]
}

proc CPz1 {rf phase {len 0}} {
  global par
  set p90 [expr 1e6/360*90/$par(rf0)]
  set p240 [expr 1e6/360*240/$par(rf0)]
  if { $len == "length" } {return [expr 2*$p90+$p240]}
  pulse $p90 $rf [expr 0+$phase]
  pulse $p240 $rf [expr 90+$phase]
  pulse $p90 $rf [expr 0+$phase]
}

proc CPz2 {rf phase {len 0}} {
  global par
  set p90 [expr 1e6/360*90/$par(rf0)]
  set p180 [expr 1e6/360*180/$par(rf0)]
  if { $len == "length" } {return [expr 2*$p90+$p180]}
  pulse $p90 $rf [expr 90+$phase]
  pulse $p180 $rf [expr 0+$phase]
  pulse $p90 $rf [expr 90+$phase]
}

proc pulseseq {} {
  global par
  matrix set 1 operator Ilz
  matrix set 2 coherence {{ +1 } {-1 }}

  if {$par(inversion)=="APz"} {
    # prepare philist and amplist stored in ilist
    set par(ilist) [eval APz $par(rf0) 0 1]
  }
  set t90 [expr 0.25e6/$par(rf0)]
  set lenCPx [eval $par(refocus) $par(rf0) 0 length]
  set delEcho [expr 2e3-($t90+$lenCPx)/2]

  foreach rf $par(rflist) {

    reset
    pulse $t90 $rf 90
    delay $delEcho
    eval $par(refocus) $rf $par(refPhase)
    delay $delEcho
    pulse $t90 $rf 90
    eval $par(inversion) [expr $rf] $par(invPhase)
    acq
  }
}

proc main {} {
  global par

```

```

set par(inversion) Px180
set par(refocus) Px180
set par(rflist) ""
for {set rf [expr 70000/2.0]} {$rf<=[expr 130000/2.0]} {set rf [expr $rf+2000/2.0]} {
  set par(rflist) "$par(rflist) $rf"
}
set par(np) [expr [llength $par(rflist)]]

set par(isolist) ""
for {set iso -30000} {$iso<=30000} {set iso [expr $iso+2000]} {
  set par(isolist) "$par(isolist) $iso"
}
set par(csalist) ""
for {set csa 0} {$csa<=40000} {set csa [expr $csa+2000]} {
  set par(csalist) "$par(csalist) $csa"
}

    foreach csa $par(csalist) {
foreach par(refocus) { Px180 CPx1 CPx2} {
  foreach par(inversion) {Px180 CPz1 CPz2 APz } {
    foreach par(refPhase) { 0 180 } {
      foreach par(invPhase) { 0 180 90 270 } {
        set res_name "$par(name)-$par(refocus)_$par(refPhase)-
$par(inversion)_$par(invPhase)-csa=$csa.res"
        puts $res_name
        set File [open $res_name w]
        foreach iso $par(isolist) {
          set f [fsimpson [list [list shift_1_iso $iso] [list shift_1_aniso $csa] ]]
          for {set i 1} {$i <= $par(np)} {incr i} {
            set Sr [expr [findex $f [expr $i] -re ] /0.5 *100]
            set Si [expr [findex $f [expr $i] -im ] /0.5 *100]
            puts $File "[expr [lindex $par(rflist) [expr $i-1]]/1000] [expr $iso/1000]
$Sr $Si"
          }
          puts $File ""
          funload $f
        }
        close $File
      }
    }
  }
}
}
}
}

```

References

- [1] D.I. Hoult, R.E. Richards, The Signal-to-Noise Ratio of the Nuclear Magnetic Resonance Experiment, *J. Magn. Reson.* 85 (1976) 71–85.
- [2] A.J. Shaka, A. Pines, Symmetric phase-alternating composite pulses, *J. Magn. Reson.* 71 (1987) 495–503. doi:10.1016/0022-2364(87)90249-6.
- [3] R. Tycko, A. Pines, Spatial localization of NMR signals by narrowband inversion, *J. Magn. Reson.* 60 (1984) 156–160. doi:10.1016/0022-2364(84)90042-8.
- [4] M.H. Levitt, R. Freeman, NMR population inversion using a composite pulse, *J. Magn. Reson.* 33 (1979) 473–476. doi:10.1016/0022-2364(79)90265-8.
- [5] M.H. Levitt, Symmetrical composite pulse sequences for NMR population inversion. I. Compensation of radiofrequency field inhomogeneity, *J. Magn. Reson.* 48 (1982) 234–264. doi:10.1016/0022-2364(82)90275-X.
- [6] S. Wimperis, Broadband, Narrowband, and Passband Composite Pulses for Use in Advanced NMR Experiments, *J. Magn. Reson. A.* 109 (1994) 221–231. doi:10.1006/jmra.1994.1159.
- [7] Z. Starčuk, V. Sklenář, Composite pulse sequences with variable performance, *J. Magn. Reson.* 62 (1985) 113–122. doi:10.1016/0022-2364(85)90301-4.
- [8] R. Freeman, S.P. Kempell, M.H. Levitt, Radiofrequency pulse sequences which compensate their own imperfections, *J. Magn. Reson.* 38 (1980) 453–479. doi:10.1016/0022-2364(80)90327-3.

